

Graphene Carrier Transport Theory

Shaffique Adam

Center for Nanoscale Science and Technology, National Institute of Standards and Technology, Gaithersburg, Maryland 20899-6202, USA
shaffique.adam@nist.gov

Abstract. This chapter describes the theory of carrier transport in two dimensional graphene sheets. At high carrier density, the conductivity of graphene depends on carrier density, the dielectric constant of the substrate and the properties of the impurity potential, which can all be treated using the Boltzmann transport formalism. At low carrier density, disorder causes the local random fluctuations in carrier density to exceed the average density. As a consequence, the carrier transport at the Dirac point is highly inhomogeneous. The ensemble averaged properties of these puddles of electrons and holes are described by a self-consistent theory, and the conductivity of this inhomogeneous medium is given by an effective medium theory. Comparing this transport theory with the results of representative experiments rigorously tests its validity and accuracy.

12.1 Introduction

Graphene has emerged as an exciting new material with remarkable technological promise and fascinating theoretical possibilities. On the materials front, graphene is the strongest measured material [1], has demonstrated superiority over conventional materials for high frequency applications [2] and has the highest phonon-limited mobility at room-temperature of any known semiconductor [3]. It was recently demonstrated that graphene is a cheap and versatile transparent conductor suitable for touch-screen and solar cell applications [4]. On the theoretical front, among many exciting proposals, graphene's Weyl-Dirac description gives rise to: a quantum critical Dirac point where perfectly clean graphene at zero temperature has no intrinsic length scale (see e.g. Ref. [5]); a topological symmetry that enables graphene to evade Anderson localization in the absence of a magnetic field [6–8]; and the possibility for the emergence of novel quantum states [9]. But at the heart of graphene studies and its subsequent electronic applications is to understand and explain the first measurements [10–13] of carrier transport in these single-atom-thick planar sheets of carbon atoms.

The electronic structure of graphene was discussed in Ch. 8. The subject of this chapter is to understand the transport mechanisms in these 2D graphene sheets. The result is a complex interplay of weak disorder, weak electron-electron interactions and some quantum mechanics that conspire together to give the constant mobility at high carrier density and the minimum conductivity plateau at low density [14].

The purpose of this chapter is not to be a review of the graphene transport literature; indeed, three such reviews became available recently [15–17], and all of the material covered here can be found in either Ref. [15] or Ref. [18], which provide the full context, history and shortcomings of this work as well as a comprehensive comparison with alternative theoretical approaches. Nor is this intended to be a substitute for the original literature; rather, it is a presentation of the main concepts leading up to the calculation of graphene’s conductivity in a coherent and pedagogical manner, providing extended details (beyond those available in the terse format of the original articles) so that a motivated graduate student could reproduce the calculations, while simultaneously highlighting with broad strokes the essential insights that motivated those calculations.

Our starting point is to appreciate that theoretical studies [19, 20] antedating graphene’s discovery predicted that graphene should have a universal minimum conductivity at zero carrier density and a density independent, but disorder dependent conductivity at high density. The first transport experiments in graphene [10–13] completely defied both these expectations: the minimum conductivity, while finite, showed significant sample-to-sample fluctuations, and at high carrier density, the conductivity increased linearly with carrier density.

While some questions still remain, we now more-or-less understand these trends quantitatively. The theory relies on three important concepts that make up the core of this chapter. First, graphene’s linear dispersion gives rise to quite unusual screening properties. In Sec. 12.2.1, screening is treated within the Random Phase Approximation (RPA), where one finds [21–24] that graphene behaves like a metal at distances longer than the Fermi wavelength and like an insulator at shorter distances. It is this unusual screening, for example, that results in the inability of graphene to screen out long-range impurity potentials such as charged Coulomb impurities. In this context, the rest of Sec. 12.2 discusses the semiclassical Boltzmann transport theory for different impurity models including screened charged impurities [14, 21, 25, 26], Yukawa potentials [27, 28], screened short-range scatterers [29] and midgap states [30], concluding that charged impurities are likely to be the dominant scattering mechanism in current transport experiments using exfoliated graphene on insulating substrates.

The self-consistent approximation [14] to describe the ground-state properties of graphene close to the Dirac point is presented in Sec. 12.3.1. At low carrier density, the disorder induced fluctuations in the local carrier density become larger than the average density. The system breaks up into inhomoge-

neous regions with varying carrier density, commonly referred to as electron and hole puddles (see Ch. 15 for a discussion of the p-n junctions that form at the interface of these puddles).

For short-range disorder, this gives rise to an effective carrier density that scales as the square-root of the areal density of impurities, while for charged impurities, the problem needs to be solved self-consistently. By mapping the screened potential onto a Gaussian model, we can solve for all statistical properties of the electron and hole puddles including their root-mean-square carrier density and the typical size of a puddle [31]. We show that the predictions of the self-consistent approximation [14] are in good agreement with numerical density functional theory results [32, 33] as well as local spectroscopic probes of graphene [34–37].

In Sec. 12.3.2 we discuss electron transport in this inhomogeneous potential using an effective medium theory [38–40]. This is a systematic technique to obtain the conductivity of an inhomogeneous material by mapping it onto a uniform system with the same conductivity. This allows us to describe the full crossover from the Dirac point, where fluctuations dominate the transport to high carrier density, where these fluctuations are irrelevant. In Sec. 12.3.3 we discuss the transport properties at finite temperature, by including the activated transport in both the electron and hole regimes; and in a finite magnetic field. In Sec. 12.3.4 we study the quantum transport in graphene [7] assuming the Gaussian correlated impurity model. By comparing a fully quantum-mechanical numerical calculation of the conductivity to the semi-classical Boltzmann transport theory, we find that while the two theories are incompatible at weak disorder, they are compatible for strong disorder [41]. This result elucidates why quantum corrections are small and the semi-classical transport theory should dominate in the experimentally relevant regime. By combining these four concepts (i.e. graphene screening, Klein tunneling, the self-consistent approximation and the effective medium theory), we summarize our results in Sec. 12.3.5 and demonstrate that four distinct features of the graphene transport measurements, namely, (i) the shift of the Dirac point (or charge neutrality point) to a non-zero applied back-gate voltage; (ii) the carrier mobility at high density; (iii) the value of the minimum conductivity and (iv) the width of the minimum conductivity plateau are all captured by the theory, which depends on only two experimentally tunable parameters (n_{imp} , which is the areal density of charged impurities, and r_s , which is the effective fine structure constant in graphene determined by its dielectric environment).

Finally, in Sec. 12.4 we discuss a sample of three representative experiments that confirm the predictions of the theory. The first looks at magnetotransport data taken from the Manchester group [42] where we demonstrate that having fixed n_{imp} from the transport data at zero magnetic field, one gets agreement at weak field for both $\rho_{xx}(B)$ and $\rho_{xy}(B)$ without introducing any additional parameters [43]. We then compare the predictions for $\sigma_{\text{min}}(n_{\text{imp}})$ with several of the early experiments in the literature including data from Columbia

group [13] where they found samples with over an order-of-magnitude variation in the sample mobility, and from Maryland group [44] where they directly tuned n_{imp} by adding potassium impurities to graphene in ultra-high vacuum. Finally, we discuss a third experiment, where r_s was tuned by depositing several monolayers of ice on top of the graphene sheet [28] providing a parameter-free test of the theoretical predictions. Our main conclusion is that these experiments (and others) have shown remarkable agreement with the theoretical predictions discussed in this chapter.

12.2 Graphene Boltzmann transport

The derivation of the semi-classical Drude-Boltzmann transport formalism can be found in several solid state textbooks [45, 46] and is basically a way of calculating the scattering time τ by accounting for the charge flow into and out of momentum eigenstates of the disorder-free system caused by the scattering potential. The formalism is considered semi-classical because the carrier dynamics are assumed to be a classical diffusion process between scattering centers, but the scattering is assumed to be quantum mechanical (where for weak disorder, for example, is calculated within the Born approximation¹). For our purposes, this is equivalent to the the leading order diagrammatic expansion for the current-current correlation function within the Kubo formalism in the limit of either vanishing disorder, or when $k_F \ell \gg 1$, where k_F is the Fermi momentum and $\ell = v_F \tau$ is the mean free path.

The result is often expressed as the Einstein relation $\sigma = e^2 \nu(E_F) D$, where $\nu(E_F) = 2_s 2_v |E_F| / (2\pi \hbar^2 v_F^2)$ is the density of states at the Fermi energy (only electrons close to the Fermi energy are involved in transport), and $D = v_F^2 \tau / 2$ is the diffusion constant in two dimensions. The “classical” contribution to the conductivity is therefore

$$\sigma = \frac{2_s 2_v e^2}{2\hbar} k_F \ell, \quad (12.1)$$

where 2_s accounts for spin degeneracy, and considering the two graphene valleys as decoupled gives 2_v .

The total conductivity, taking into account the next leading order in $k_F \ell$ includes “quantum corrections” $\Delta\sigma = \pm [2_s 2_v e^2 / (\pi \hbar)] \ln(L/\ell)$ that we discuss in Sec. 12.3.4 below. The Boltzmann transport theory gives the mean free path $\ell = v_F \tau$ as

$$\frac{\hbar}{\tau} = 2\pi n_{\text{imp}} \sum_{\mathbf{k}'} \left| \frac{V(q)}{\epsilon(q)} \right|^2 F(\theta) \frac{1 - \cos(\theta)}{2} \delta(E_F - \epsilon_{\mathbf{k}'}). \quad (12.2)$$

¹ The Born approximation treats the scattering potential to leading order. It is not obvious that attempts to go beyond the approach presented here have provided a more accurate solution (see discussion in Ref. [15] and Ref. [41]). A critique of the Born approximation can be found in Ref. [17] and Ref. [47].

The derivation of this equation is a straight forward extension of the usual case and will not be done here. Instead we briefly define all the terms and motivate their origin. n_{imp} is the two dimensional areal density of impurities. As alluded to above, one can obtain this “classical” limit by considering the case of vanishing impurity concentration, and the leading order term is therefore linear in n_{imp} . Built into Eq. 12.2 is the assumption that the impurities are uncorrelated and the concentration is dilute enough so that processes involving multiple scattering off the same impurity are smaller than the single scattering process. The δ -function guarantees energy conservation and requires that only the electrons at the Fermi energy participate in the transport, while $q = |\mathbf{k} - \mathbf{k}'|$ is the momentum transfer between incoming plane-waves with wave vector \mathbf{k} and outgoing wavefunctions with wavevector \mathbf{k}' . Note, \mathbf{k} and \mathbf{k}' lie on different points of the circular Fermi surface of radius k_F thereby defining the scattering angle $\theta = \theta_{kk'}$.

What is different for graphene is the “chirality factor” $F(\theta)$ which arises from the fact that the eigenvectors of the Dirac Hamiltonian are plane waves multiplied by spinors that for momentum states given by k_x and k_y depend only on the angle $\theta_{\mathbf{k}} = \arctan(k_y/k_x)$. Computing the overlap between incoming and outgoing states involves an overlap of the spinor parts of the wavefunction, which gives $F(\theta) = [1 + \cos(\theta)]/2$ for Dirac fermions [21, 25, 26]. A little bit of algebra gives

$$\frac{\hbar}{\tau} = \frac{4}{\pi} \frac{k_F}{v_F} \int_0^1 d\eta \eta^2 \sqrt{1 - \eta^2} \left| \frac{V(2k_F\eta)}{\epsilon(2k_F\eta)} \right|^2, \quad (12.3)$$

where $V(q = 2k_F\eta)$ is the bare scattering potential and $\epsilon(q = 2k_F\eta)$ is the static dielectric function that accounts for the screening by electrons. It should be clear from Eq. 12.3 that the nature of both the impurity potential and the screening function can have a major impact on graphene conductivity. For example, for unscreened Coulomb scatterers where $V(q) \sim q^{-1}$, we see that $\tau \sim k_F$ implying that for fixed impurity concentration, the mean free path gets smaller (and vanishes) as one approaches the Dirac point (i.e. $k_F \rightarrow 0$), whereas for unscreened delta-correlated scatterers defined here as having $V(q) \sim q^0$, we get $\tau \sim 1/k_F$ and the mean free path gets larger (and diverges) as one approaches the Dirac point. This strong dependence on impurity type that follows directly from applying the rules of the semi-classical Drude-Boltzmann formalism to graphene can seem counter-intuitive to those more familiar with transport in conventional 2D systems (the same result is obtained using diagrammatic perturbation theory or Green’s functions methods).

The contribution from screening can also seem unusual. As we shall see below, it turns out, by pure coincidence, that for graphene the Thomas-Fermi (TF) result is reproduced in the Random Phase Approximation (RPA) even for $q \neq 0$. (For $q = 0$ the agreement between RPA and Thomas-Fermi is guaranteed by the compressibility sum rule). Within the TF approximation, we have that $\epsilon(q, k_F)$ depends on the ratio $\eta = q/(2k_F)$ as

$$\epsilon(\eta) = 1 + V(q = 2k_F\eta)\nu(E_F) = 1 + 2r_s/\eta, \quad (12.4)$$

where $r_s = e^2/(\kappa\hbar v_F)$ is the gas parameter defined as the ratio of potential energy to kinetic energy, which measures the relative strength of the electron-electron interactions. Equivalently, r_s can be thought of as the effective “fine-structure constant” or coupling constant for interacting Dirac fermions. We note in passing that for a parabolic dispersion $r_s \sim k_F^{-1}$ so that low carrier density heralds the strongly interacting regime, while for graphene’s linear dispersion $r_s \approx 2/\kappa \leq 2$, is density independent.²

One interesting and perhaps unexpected effect is the opposite role of dielectric screening for Coulomb and short-range impurities. One notices that increasing the dielectric screening of the environment (i.e. increasing κ or decreasing r_s) *decreases the conductivity* for delta-correlated impurities where $V(q) \sim q^0$. This is because decreasing r_s reduces the electron-electron interactions and therefore the ability of the electron gas to screen the impurity potential, making the disorder potential appear stronger than before. In sharp contrast, for Coulomb scatterers where $V(q) \sim e^2/(\kappa q) \sim r_s/q$, decreasing r_s weakens the impurity potential thereby *increasing the conductivity*.

While the discussion so far has been somewhat qualitative, the goal for the remainder of this section is to be more quantitative. The semiclassical transport result (Eq. 12.3) depends on the interplay between the impurity potential $V(q)$ and the screening properties of graphene electrons. We will first discuss the calculation of $\epsilon(q)$ within the RPA, followed by the calculation of the conductivity with different choices for the disorder potential $V(q)$.

12.2.1 Screening: Random Phase Approximation (RPA)

In the modern context³, the RPA approximation is usually understood in terms of a diagrammatic expansion for the electron gas self-energy (see Refs. [45, 46]). Within the RPA, the dielectric function is related to the polarizability as $\epsilon(q) = 1 + V(q)II(q)$ (see right panel of Fig. 12.1), where $II(q)$ (left panel of Fig. 12.1) is the polarizability function (or “pair-bubble”). The goal of this section is to calculate the pair-bubble for graphene. We now know

² Here κ is the average of the dielectric constants of the medium above and below the graphene sheet, and the numerical coefficient (≈ 2) is a material parameter set by the overlap of the carbon π -orbitals in the honeycomb lattice and the separation between the carbon atoms set by the σ -bonds.

³ Historically, the RPA was introduced by Bohm and Pines when discussing the plasma oscillations of the electron gas in the high density limit. In that context, the approximation corresponds to looking at the Fourier transform of the potential energy and showing that after subtracting the term that was linear in carrier density, the sub-leading term had sums over the phase of electrons that depended on their position. Averaging over position gave a highly oscillatory summand that would be negligible or equivalent to the vanishing of that sum for random electron phases.

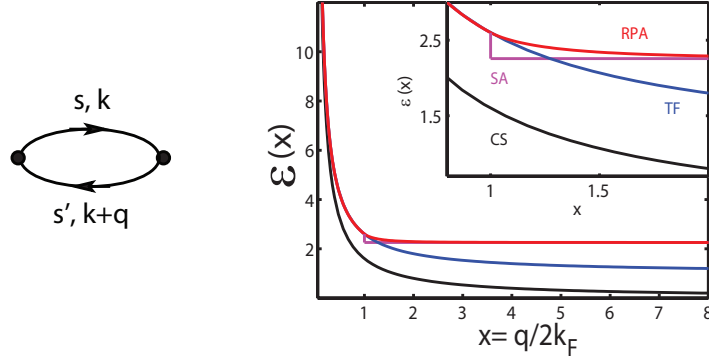


Fig. 12.1. Left panel shows diagrammatic representation of the polarization bubble corresponding to Eq. 12.5. The right panel shows different dielectric functions used in the literature, including the “Complete Screening” (CS), “Thomas-Fermi” (TF) and “Random Phase Approximation” (RPA). The inset shows a blow-up at $q = 2k_F$ to show how the “Step Approximation” (SA) given by Eq. 12.10 differs from the exact result Eq. 12.9.

that both the inter-band and intra-band contributions are important. Historically, the inter-band contribution was derived much earlier [48] while the full solution for the graphene polarizability appeared only after the discovery of graphene [21–24]. Here we follow the derivation by Hwang and Das Sarma (Ref. [22]).

The polarizability function (see Fig. 12.1) is given by

$$\Pi(q) = \frac{2_s 2_v}{L^2} \sum_{k, s, s'} \frac{f_k^s - f_{k'}^{s'}}{\varepsilon_{s, k} - \varepsilon_{s', k'}} \frac{1 + s s' \cos \theta_{k, k'}}{2}, \quad (12.5)$$

where f_k is the Fermi distribution, and what is different for graphene is the sum over both electron bands ($s = 1$) and hole bands ($s = -1$) and the overlap between the spinor components of the wavefunction (see Ref. [21] for more details). Expanding the sum over band-indices s, s' , one can group the terms involving f^+ and f^- separately calling the former Π_+ and the later Π_- , where $\Pi(q) = \Pi^+(q) + \Pi^-(q)$. This grouping is especially useful since at zero temperature $f_k^+ = \theta(k_F - k)$ and $f_k^- = 1$. One notices that the term $\Pi^-(q)$ is just the contribution from a completely filled valence band and a completely empty conduction band (which is also called “intrinsic graphene”), while the term $\Pi^+(q)$ is the polarizability of, for example, a partially filled electron band ignoring the valence band. (Particle-hole symmetry means that it is the same for an empty conduction band with a valence band partially filled with holes. For simplicity, we assume that $E_F > 0$, where the corresponding results

for $E_F < 0$ are identical). The intrinsic polarizability is given by⁴

$$\Pi^-(q) = \frac{2_s 2_v}{\hbar v_F} \int \frac{d^2 k}{(2\pi)^2} \frac{1 - \cos \theta}{|k| + |k + q|} = \frac{2_v 2_s q}{16 \hbar v_F}. \quad (12.7)$$

Since the intrinsic polarizability is proportional to q , one can immediately see that the dielectric function becomes independent of q , i.e. $\epsilon(q) = 1 + r_s \pi/2$. This result remains correct whenever $q \gg 2k_F$, where one can then approximate the graphene polarizability as that of intrinsic graphene. At these large momenta (or small distances) the existence of a completely filled valence band means that graphene screens like a dielectric insulator.

In contrast, the contribution $\Pi^+(q)$ is metallic in nature (this is because particle-hole excitations around the Fermi circle are constrained by the compressibility sum rule, and these are bounded by the bottom of the conduction band). To calculate $\Pi^+(q)$, one first notices that the terms that involve $f_{k'}^+$ are related to those with f_k^+ by a change of variable where $\Pi^+(q) = \Pi_1^+(q) + \Pi_1^+(-q)$, and

$$\begin{aligned} \Pi_1^+(q) &= \frac{2_s 2_v}{\hbar v_F} \int \frac{d^2 k}{(2\pi)^2} \theta(k - k_F) \frac{|k| + |k + q| \cos \theta_{kk'}}{(|k| + |k + q|)(|k| - |k + q|)}, \\ &= \frac{2_s 2_v}{4 \hbar v_F \pi} \left[1 + \frac{k_F}{2\pi} \int_0^{k_F} dk \int_0^{2\pi} d\phi \frac{4k^2 - q^2}{q^2 - 2kq \cos \phi} \right]. \end{aligned} \quad (12.8)$$

For $|q| < 2k_F$ the integral gives $-\pi|q|/8$ and this contribution to Π^+ exactly cancels the intrinsic contribution from Π^- , so that the Thomas-Fermi result $\Pi(q) = \nu(E_F) = 2k_F/(\pi \hbar v_F)$ works beyond the $q \rightarrow 0$ limit.⁵ Introducing the variable $x = q/2k_F$ and putting everything together, the graphene polarizability is

$$\frac{\Pi(q = 2k_F x)}{\nu(E_F)} = \begin{cases} 1, & \text{for } x \leq 1 \\ 1 + \frac{\pi x}{4} - \frac{x}{2} \arcsin\left(\frac{1}{x}\right) - \frac{1}{2x} \sqrt{x^2 - 1}, & \text{for } x \geq 1. \end{cases} \quad (12.9)$$

This coincidence of $\Pi(q)/\nu(E_F) = 1$ for $q \leq 2k_F$ also holds for the 2D electron gas [49] but it is not universally true, *e.g.* it doesn't hold for graphene bilayers (see discussion in Ref. [15]). Moreover, as we shall see in Sec. 12.3 below, the Thomas-Fermi and RPA screening approximations give quantitatively different results for the disorder-induced potential fluctuations and the

⁴ The integral can be done by making the substitution $x = |k| - |k + q|$ and noticing that

$$k dk = \frac{1}{2} \frac{x^2 - q^2}{x + q \cos \theta_{kq}} \frac{dx}{1 - \cos \theta_{kk'}}. \quad (12.6)$$

⁵ The fact that $\Pi(q) = \nu(E_F)$ for $q \leq 2k_F$ implies that for high-density *transport properties*, the Thomas-Fermi approximation and the RPA give the same results (notice that Eq. 12.3 only integrates the dielectric function from 0 to $2k_F$), where $\epsilon(q \leq 2k_F) = 1 + V(q)\Pi(q) = 1 + q_s/q$.

resulting graphene minimum conductivity at low carrier density. In this case, we will need the full dielectric function $\epsilon(q) = 1 + V(q)\Pi(q)$ which can readily be obtained from Eq. 12.9. However, since in such cases we are typically integrating $\epsilon(q)$ over all q , the full RPA result is indistinguishable from the following Step Approximation (SA) for the dielectric function [14]

$$\epsilon(q) = \begin{cases} 1 + \frac{q_s}{q}, & \text{for } q \leq 2k_F \\ 1 + \frac{r_s\pi}{2}, & \text{for } q > 2k_F. \end{cases} \quad (12.10)$$

The graphene dielectric function is shown in Fig. 12.1 where we compare the Step Approximation (SA) given by Eq. 12.10 with the Thomas-Fermi (TF), RPA, and Complete Screening (CS) approximations. In this context, the CS approximation corresponds to the assumption $\epsilon(q) = q_s/q$, which can be thought of as the TF approximation with the additional assumption that $q_s \gg q$. However, for monolayer graphene since $r_s \leq 2$ and $q_s = 4k_F r_s$, the condition $q \sim 2k_F \ll 4k_F r_s$ is never realized.

12.2.2 Coulomb scatterers

Having established that Eq. 12.3 and Eq. 12.4 remain valid within the RPA, one can then calculate the transport properties of various scattering potentials. We begin with long-range Coulomb potentials. Taking the 2D Fourier transform of a charged impurity displaced by a distance d from the 2D plane in a medium with dielectric constant κ , we get

$$V(q) = \frac{2\pi e^2}{\kappa} \frac{e^{-qd}}{q}. \quad (12.11)$$

Solving Eq. 12.3 gives $\sigma(n, n_{\text{imp}}, r_s, d)$. The effect of increasing d is to slightly increase the conductivity from the $d = 0$ value [26]. For $d \approx 1$ nm, it is sufficient to use the result for $d = 0$, in which case, an analytic solution for $\sigma(n, n_{\text{imp}}, r_s, d = 0)$ can be obtained

$$\sigma = A[r_s] \frac{e^2}{h} \frac{n}{n_{\text{imp}}} = 20 \frac{e^2}{h} \frac{n}{n_{\text{imp}}} \quad \text{for } r_s = 0.8. \quad (12.12)$$

The function $A[r_s]$ is shown in Fig. 12.2. To be consistent with the notation in the original literature, we express $A[r_s] = F_1[x = 2r_s]^{-1}$, and

$$\frac{F_1(x)}{x^2} = \frac{\pi}{4} + 3x - \frac{3x^2\pi}{2} + x(3x^2 - 2) \frac{\arccos[1/x]}{\sqrt{x^2 - 1}}. \quad (12.13)$$

As anticipated in the discussion below Eq. 12.4, $A[r_s]$ is a monotonically decreasing function (see Fig. 12.2) implying that increasing the dielectric constant of the substrate would increase the graphene mobility provided the new substrate had a similar number of charge traps. Similarly, for suspended graphene, one “loses” about a factor of 2 from the decrease of $A[r_s]$, but since by current annealing the sample, one can reduce the impurity density by more than an order of magnitude, one can still drastically improve the carrier mobility [50, 51].

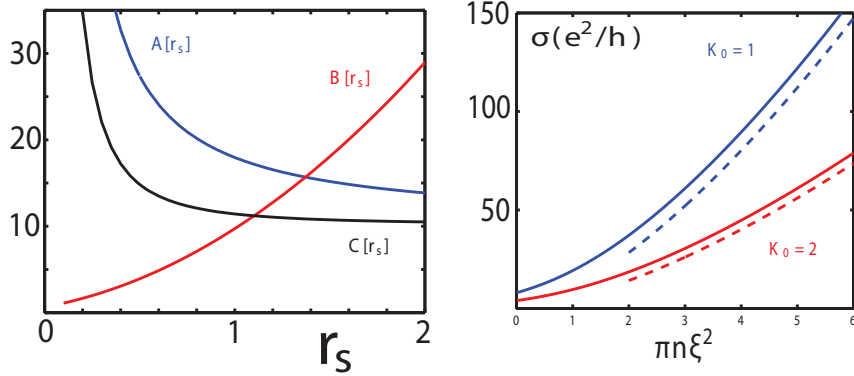


Fig. 12.2. High-density graphene conductivity for different impurity models. Left panel: Dimensionless coefficients that determine the dependence of the high-density conductivity on graphene's effective fine-structure constant r_s (see text for details). For charged impurities, $\sigma = A[r_s](e^2/h)(n/n_{\text{imp}})$, while for delta-correlated impurities $\sigma = B[r_s](e^2/h)\sigma_0$. Yukawa-like disorder behaves qualitatively like charged impurities, $\sigma = C[r_s](e^2/h)(n/n_{\text{imp}})$, although as seen in the figure, there are quantitative differences. Right panel: Conductivity for the Gaussian correlated impurity model as a function of $\pi n \xi^2$ for $K_0 = 1$ and $K_0 = 2$. Dashed lines are the high density asymptote $\sigma = (2\sqrt{\pi}e^2/K_0h)(2\pi n \xi^2)^{3/2}$.

12.2.3 Gaussian white noise disorder

White noise disorder is the most common approximation made when discussing the conductivity of the regular 2D electron gas. One simply assumes that $V(q)$ is a constant (*i.e.* independent of q). Mathematically, this corresponds to uncorrelated impurities each expressed as a delta-function in real space *i.e.* $V_{\text{tot}}(r) = u_0 \sum_{i=1}^N \delta(r - r_i)$, where the impurities are located at positions r_i with zero range. Physically, this could correspond to atomically sharp defects such as dislocations or missing atoms (although when calculating their effect on the conductivity, here we neglect any intervalley transitions). Solving Eq. 12.3, we find $\sigma = B[r_s]\sigma_0$, where σ_0 is a constant proportional to $(n_{\text{imp}}u_0^2)^{-1}$ and $B[r_s] = (F_2[x = 2r_s])^{-1}$, where

$$F_2(x) = \frac{\pi}{2} - \frac{16x}{3} + 40x^3 + 6\pi x^2 - 20\pi x^4 + 8x^2(5x^3 - 4x) \frac{\arccos[1/x]}{\sqrt{x^2 - 1}}. \quad (12.14)$$

The function $B[r_s]$ is shown in Fig. 12.2. We note that as discussed earlier, $B[r_s]$ is a monotonically increasing function of r_s since dielectric screening makes the impurity potential look weaker at larger r_s resulting in a larger conductivity. Also, the functions $A[r_s]$ and $B[r_s]$ are real and positive for all values of $r_s > 0$ (*i.e.* the ratio of $\arccos(1/x)$ and $\sqrt{x^2 - 1}$ is real, even for values of $x < 1$).

12.2.4 Yukawa potential

In principle, one could calculate the screening properties for any scattering potential. By comparison with experiment where the dielectric environment is changed (see Sec. 12.4 below), one could then establish definitively the nature of the disorder impurity potential. In 3D, the Yukawa potential (in real space) is the Fourier transform of the screened Coulomb potential (in momentum space). However, in 2D we have been unable to obtain a closed-form analytic expression for the screened Coulomb potential in real-space. Instead, one could solve for the Boltzmann conductivity for the phenomenological Yukawa potential where

$$\frac{V(q)}{\epsilon(q)} = \frac{2\pi e^2}{\kappa} \frac{1}{\sqrt{q^2 + q_s^2}}, \quad (12.15)$$

to find $\sigma = C[r_s](e^2/h)(n/n_{\text{imp}})$, where $C[r_s] = (F_3[x = 2r_s])^{-1}$ and

$$\frac{F_3(x)}{x^2} = \frac{\pi}{4} + \frac{\pi x^2}{2} - \frac{\pi x}{2} \sqrt{1 + x^2}. \quad (12.16)$$

Qualitatively, the Yukawa potential behaves similarly to the screened Coulomb potential, but there are quantitative differences. For example, at $r_s = 0.8$, for the same number of impurities, a graphene sample with Yukawa-like disorder would have about half the mobility compared to the screened Coulomb potential. The experiments along the lines discussed in Sec. 12.4 where n_{imp} or r_s is tuned in a controlled fashion can discriminate between the two models.

12.2.5 Gaussian correlated impurities

A very popular choice for impurity potential in graphene is the Gaussian correlated potential where

$$\langle V(r)V(r') \rangle = K_0 \frac{(\hbar v_F)^2}{2\pi\xi^2} e^{-|\mathbf{r}-\mathbf{r}'|/(2\xi^2)}. \quad (12.17)$$

This potential has two parameters: K_0 is a dimensionless measure of the potential strength and ξ specifies its correlation length. The reason for its wide use is both theoretical and practical – First, by looking at the dependence on ξ one can study the crossover from short-range to long-range impurity behavior [52]. Second, the limit $n \rightarrow 0$ for $\xi = 0$ is somewhat uncontrolled in several respects. Without going into the details, we just point out, as we shall see below, that many physical quantities (such as the conductivity) depend on the quantity $n\xi^2$ and so keeping a finite ξ allows one to take the limit $n \rightarrow 0$. And finally, unlike the long-range Coulomb potential that can introduce spurious divergences in finite sized numerics, a finite ξ makes these computations more convergent. There are also some experimental indications that atomic

hydrogen dopants in graphene give changes to the conductivity that are consistent with the predictions of this Gaussian correlated impurity model [53]. We assume here that the values of K_0 and ξ are for a screened impurity potential (see Sec. 12.3.1 below where we give expressions for $K_0[r_s]$ and $\xi[r_s]$ for a particular mapping of the Coulomb potential). Integrating Eq. 12.3 for this model, we find [41]

$$\sigma(K_0, x = n\xi^2) = \frac{4e^2}{h} \frac{x e^x}{K_0 I_1(x)}, \quad (12.18)$$

where I_1 is the modified Bessel function. Two points are worth making here: (i) For large carrier density $x \gg 1$, the conductivity is super-linear $\sigma \sim n^{3/2}$; and (ii) In the limit $n \rightarrow 0$, the conductivity remains finite (see Fig. 12.2), although in Sec. 12.3.4 we argue that this is not the origin of the graphene minimum conductivity even for this choice of impurity potential.

12.2.6 Midgap states

An increasingly popular choice (See e.g. Refs. [17, 30, 54, 55]) for modelling graphene impurities is the so-called midgap states or resonant scatterer model. Unlike the other forms of disorder we have examined, where we assume that the disorder is a small perturbation to the pristine case, these works consider the impurities to be strong enough to generate extra structure in the density of states. In the unitary limit (*i.e.* assuming that the impurities create a maximal phase-shift of $\pi/2$ between incoming and outgoing wavefunctions), one can show [30, 56]

$$\sigma(n) = \frac{2e^2}{\pi h} \frac{n}{n_{\text{imp}}} \ln^2 [\sqrt{\pi n R}], \quad (12.19)$$

where R is the scattering radius of the impurity and n_{imp} is the concentration of resonant scatterers. As a function of carrier density, the graphene conductivity in the midgap model looks linear at low carrier density, and is sublinear at high density, quite similar to the case when one considers the presence of both Coulomb scatterers and short-range scatterers. Although both of these scenarios have two adjustable parameters, it is nonetheless possible to distinguish them experimentally. Indeed, in experiments on graphene irradiated with ions [57] it appears that the midgap states model better captures the experimentally observed $\sigma(n, n_{\text{imp}})$ than the combination of weak Coulomb and short-range scatterers. Whereas for most other samples, the combination of weak scatterers seems to dominate (see Sec. 12.4).

For the purposes of this chapter, we would like to make three cautionary remarks about this impurity model: (i) In the range between weakly interacting impurities (*i.e.* Born approximation) and the case of unitary scatterers is the whole spectrum of strong but not unitary impurities. While the theory of unitary scatterers might be tractable, there is no reason why nature would

choose this particular limit. (ii) Resonant scatterers typically give a maximal phase-shift at a particular energy (and hence the name), but provide only weak scattering away from this resonant energy. While treating mid-gap states in graphene, it is often assumed that the impurity state is resonant over the entire energy window probed in transport. In principle, it should be possible to extract the width of the resonance by looking for changes in the conductivity as a function of r_s , although this problem has not yet been treated theoretically. (iii) There has been only very limited work (e.g. Refs. [47, 54, 58] and references therein) connecting these midgap states to the graphene minimum conductivity problem. Although this is the subject of Sec. 12.3 below, it is worth mentioning here that relying exclusively on midgap states, for example, by obtaining a residual carrier density by integrating the density of states including the structure induced by the resonant impurities, cannot explain the graphene minimum conductivity. To get the experimentally observed values of σ_{\min} requires an unphysically large number of defects (such as missing atoms). Not only would these large number of defects degrade the mobility far beyond what is observed in the same transport experiments at high carrier density, but these would most certainly be observable in scanning tunneling microscope (STM) studies, which have actually found the opposite case i.e. a very low concentration of such defects (see e.g. Ch. 3 and Refs. [9, 37, 59, 60]).

We would argue that even when samples are deliberately made to have a large number defects (e.g. by ion irradiation), the residual carrier density is still determined by the charged impurity concentration (see e.g. discussion in Ref. [57]). In such a case, where one has the combination of resonant scatterers and Coulomb scatterers using the mid-gap model (Eq. 12.19) is almost indistinguishable from the Coulomb impurity model. This is because the mid-gap model has an additional adjustable parameter R that could be tuned to get the pre-factor of the conductivity to be comparable to $A[r_s] \approx 20$ (see Fig. 12.2). In this case, the only way to distinguish mid-gap states from charged impurities is by controllably changing some parameter such r_s [28], the concentration of charged impurities [44], or the concentration of resonant scatterers [57].

12.3 Transport at low carrier density

One of the biggest puzzles that emerged from the first transport experiments on graphene was the existence of a finite conductivity at zero carrier density. It turns out that well before the discovery of graphene, it was predicted by Ref. [19] and others that there should be a universal quantum limited ballistic conductivity in clean graphene $\sigma_{\min} = (4/\pi)e^2/h$. However, the first transport experiments measured values closer to $\sigma_{\min} = 4e^2/h$. Since at that time, the observed value was widely believed to be universal, this unexpected value for the minimum conductivity in graphene was dubbed the “problem of the missing π ”.

It is the goal of this section to discuss the quantitative theoretical explanation for this problem. The short answer to this mystery is that the minimum conductivity observed in experiments is not universal, but depends on the concentration of charged impurities. For relatively dirty graphene samples, the enhanced conductivity caused by the fluctuations in carrier density induced by the disorder is roughly compensated by the increased scattering caused by those impurities. In this regime, $\sigma_{\min} \approx 4e^2/h$ and depends only weakly on the disorder concentration (although we emphasize that the value is not universal, and even dirtier samples should have a lower conductivity). For samples that are 30 times cleaner, the reduced scattering term wins, giving a *larger* value for the minimum conductivity $\sigma_{\min} = 8e^2/h$.

Indeed, later experiments [13] observed that the minimum conductivity was not universal, but varied from $\sigma_{\min} = 2e^2/h$ to $8e^2/h$ consistent with theoretical predictions [14].

For even cleaner samples, the minimum conductivity would continue to increase until either the mean-free-path becomes comparable to the sample size or the size of the puddles (i.e. carrier density fluctuations) would shrink to fewer than a couple of electrons. Then the semiclassical diffusive transport would cross over to the fully quantum ballistic regime (which we discuss in Sec. 12.3.4).

As alluded to in the introduction to this chapter, the explanation of the graphene minimum conductivity problem is an intricate symphony that brings together the physics of disorder, electron-electron interactions and quantum mechanics. Here, disorder plays a dual role: it is primarily responsible for scattering the electrons that gives rise to the finite conductivity in the first place (recall that the bulk conductivity of any 2D conductor without disorder is infinite) *and* it induces the carrier density fluctuations; so that depending on the amount of disorder, the local carrier density can be quite large, allowing, at least locally, for a non-vanishing conductivity. The relatively weak electron-electron interactions in graphene give the mechanics of how the electrons “see” the disorder potential which is invariably screened by the quasiparticle cloud, and this applies equally to both roles of disorder, as a scattering center and in inducing the density inhomogeneities. With quantum mechanics comes Klein tunneling, the ability of electrons to transmute to holes across potential barriers – which in our case implies that we do not need to worry about the scattering at the boundary between the electron and hole puddles. The contribution to the total conductivity is dominated by the conductivity *within* the puddles and not *across* them⁶.

⁶ To fully discuss the role of Klein tunneling in graphene transport would require a larger discussion than is possible here. For the semiclassical calculation presented here, we ignore the additional contribution to the resistance arising from p-n junctions. The validity of this assumption is rigorously tested in Sec. 12.3.4 below. For a more complete discussion on the role of p-n junctions in graphene transport, as well as an explanation for the remarkable property of perfect transmission of carriers at normal incidence, see Ch. 12 and Ref. [15].

We should mention that historically, this solution emerged only after carefully comparing the experimental data to the high density Boltzmann theory discussed in Sec. 12.2 above. That theory is only valid at high density, or more specifically, when $k_F \ell \gg 1$, or $\sigma(n) \gg e^2/h$. Oftentimes, either by serendipity or insight, theories work well beyond their formal limits of applicability – we have already seen that for graphene and the usual 2D electron gases, the RPA calculation showed explicitly that the Thomas-Fermi screening theory, which is valid formally only at $q \rightarrow 0$, actually works well for $q \leq 2k_F$. Similarly, the RPA-Boltzmann theory for the usual 2DEG system continues to work beyond its formal regime of applicability in high mobility n-GaAs systems [61] until new physics such as percolation or localization takes over at even lower carrier densities.

However, when a careful comparison with experiment was done in Ref. [26] to see when deviations from this semiclassical theory begin to show up, it revealed two important features that inspired the theoretical ideas presented below. First, the high density theory *did* work better than expected. From Eq. 12.12, one would expect the high density theory to work only for $n \gg n_{\text{imp}}$, but in fact, the theory worked for $n \gtrsim n_{\text{imp}}/2$. Second, the minimum conductivity value did not occur at a singular point (i.e. at the Dirac point with precisely zero carrier density), but rather there was a minimum conductivity plateau of width $\Delta n \approx n_{\text{imp}}$. In fact, there was no singularity at all – the plateau smoothly joined up to the high-density Boltzmann result and the value of the conductivity minimum was not universal, but seemed somewhat correlated with the sample quality. It was pointed out already in Ref. [26] that for $n \approx n_{\text{imp}}/2$, the fluctuations in carrier density n_{rms} were comparable to the average carrier density implying that understanding the physics of the minimum conductivity was understanding the physics of puddles i.e. how they are formed and how they conduct carriers, and had nothing to do with the properties of the peculiar Dirac point that was experimentally inaccessible due to the presence of disorder. This was significant since at the time, most attempts to explain the graphene minimum conductivity focused on the singular properties of the conical point in the graphene Dirac spectrum.⁷

⁷ To illustrate somewhat simplistically how one could get into trouble at the Dirac point, consider the Einstein relation that was discussed earlier $\sigma = e^2 \nu(E_F) D$. At the Dirac point, $\nu(E_F)$ vanishes but for short-range impurities, $D \rightarrow \infty$, which gives rise to a disorder-dependent minimum conductivity at the Dirac point (see Fig. 12.2). Similar cancellation of divergences gives rise to the following puzzle [19]. If one calculated the conductivity by first taking the clean limit while keeping either temperature or frequency finite, one would obtain the universal value $\sigma_{\text{min}} = (\pi/2)e^2/h$. However, taking frequency and temperature to zero first, then taking the clean limit gives $\sigma_{\text{min}} = (4/\pi)e^2/h$. At the time of writing, the crossover between these two universal limits remains an unsolved problem. However, for the purposes of understanding current graphene dc transport experiments, we maintain that none of this “universal” physics is relevant.

12.3.1 Self-consistent approximation

Perhaps the most important result discussed in this chapter is the self-consistent ansatz of Ref. [14]. In a nutshell, the self-consistent ansatz is a semi-analytic method for calculating the fluctuations in carrier density n_{rms} from the properties of the disorder potential. By now this ansatz has been rigorously tested against numerical density functional calculations [32] (for the case of interacting electrons) and with a numerical computation of the Landauer formula [41] (for the fully quantum mechanical case). The self-consistent ansatz states that the root-mean-square fluctuations in carrier density (n_{rms}) is related to the screened disorder potential at that carrier density.

One can think of the ansatz as follows: If the induced carrier density n_{rms} is small, the disorder potential will be poorly screened thereby inducing a large carrier density. But a large carrier density will better screen the disorder potential resulting in a lower carrier density. This process will reach an equilibrium when the changes in the induced carrier density exactly balance the changes in screening.

Formalism

To be more quantitative, let us further assume that the largest contribution to n_{rms} is the Thomas-Fermi contribution i.e. $n_{\text{rms}} \approx \sqrt{3} \langle E_{\text{F}}^2 \rangle / (\pi \hbar^2 v_{\text{F}}^2)$, where the angular brackets denote averaging over an ensemble of disorder configurations and the $\sqrt{3}$ factor just comes from the fact that for graphene n_{rms} is the second moment of density and the fourth moment of Fermi energy. In this case, the self-consistent ansatz reads

$$\pi \hbar^2 v_{\text{F}}^2 n^* = \langle E_{\text{F}}^2 \rangle = \langle V_{\text{D}}^2[n^*] \rangle. \quad (12.20)$$

This corresponds to finding a residual carrier density $n^* = n_{\text{rms}}/\sqrt{3}$ that satisfies Eq. 12.20, where $V_{\text{D}}[n^*]$ is the disorder potential screened by a homogeneous electron gas at carrier density n^* .

It should be apparent from Eq. 12.20 that it will be important to calculate the ensemble averaged properties of the screened disorder potential. For example, one can show that by assuming uncorrelated random impurities of concentration n_{imp} , where each impurity has a disorder potential $\phi(r, n)$ (with Fourier transform $\tilde{\phi}(q, n)$) then [62]

$$\langle V_{\text{D}}(r) V_{\text{D}}(0) \rangle_{\text{c}} = n_{\text{imp}} \int \frac{d^2 q}{(2\pi)^2} [\tilde{\phi}(q, n)]^2 e^{-i\mathbf{q} \cdot \mathbf{r}}, \quad (12.21)$$

where the subscript ‘c’ indicates that terms proportional to $\langle V_{\text{D}}(0) \rangle$ have been excluded. To simplify the discussion, we just set $\langle V_{\text{D}}(0) \rangle = 0$. We will discuss the case of finite doping in Sec. 12.3.2 below, but for now, we can imagine that setting $\langle V_{\text{D}}(0) \rangle = 0$ corresponds to tuning the back gate voltage to coincide with the Dirac point, thereby ensuring charge neutrality.

In this case, a more general result states that for any arbitrary disorder potential $\phi(r)$, one has

$$\langle V_D^k \rangle_c = n_{\text{imp}} \int d^2r [\phi(r, n)]^k. \quad (12.22)$$

Since knowing all moments of a distribution function is equivalent to knowing the distribution function itself, in principle, after using Eq. 12.20 to set $\phi(r, n) = \phi(r, n^*)$, Eq. 12.22 then defines the full probability distribution function of the screened disorder potential.

Taking this together with the two point correlation function (Eq. 12.21), one then has a complete statistical description of *all* properties of the Dirac point in the presence of disorder. Any physical observable, such as σ_{min} should be a function of the moments in Eq. 12.22. In practice, however, since for the screened Coulomb impurity problem no closed form analytic expression is available for $\phi(r, n)$, the moments of Eq. 12.22 can only be computed numerically, and one needs to truncate the computation after a finite number of moments.

In this vein, it is sometimes useful to consider the mapping to the Gaussian correlated disorder (see Eq. 12.17) which can be accomplished as follows

$$\begin{aligned} \frac{K_0 \hbar^2 v_F^2}{2\pi \xi^2} &= n_{\text{imp}} \int \frac{d^2q}{(2\pi)^2} [\tilde{\phi}(q, n)]^2 = \pi \hbar^2 v_F^2 n^*, \\ \xi &= \sqrt{\frac{2}{\pi}} \frac{\int \frac{dq}{2\pi} [\tilde{\phi}(q, n)]^2}{\int \frac{d^2q}{(2\pi)^2} [\tilde{\phi}(q, n)]^2}. \end{aligned} \quad (12.23)$$

While this ‘‘Gaussian mapping’’ can be done for any arbitrary potential $\phi(r, n)$, it will only be a good approximation if higher moments of the impurity potential in Eq. 12.22 can be neglected.⁸ We also find

$$n_{\text{rms}} = n^* \sqrt{3 + \frac{1}{\pi n_{\text{imp}} \xi^2}}. \quad (12.24)$$

We now specialize to the case of Coulomb impurities, where from Eq. 12.11 we have

$$\tilde{\phi}(q) = \frac{2\pi e^2}{\kappa} \frac{e^{-qd}}{q\epsilon(q)}. \quad (12.25)$$

⁸ We have been slightly sloppy with language, using the term Gaussian approximation to refer to both when the disorder potential has Gaussian two-point spatial correlation function (see Eq. 12.17) and when the disorder probability distribution function is determined only from the second moment (see Eq. 12.22). From the context it should be clear which case we mean, although we should caution that the two approximations can be quite different. For example, Eq. 12.24 describes a Gaussian two-point correlation function, but is equivalent to a Gaussian distribution function only in the limit when $n_{\text{imp}} \pi \xi^2 \gg 1$.

The dielectric function $\epsilon(q)$ was defined in Eq. 12.10. Notice that to calculate n_{rms} the integrals run over all momenta q and so, unlike the transport calculations in Sec. 12.2, the full RPA result will differ from the Thomas-Fermi result.

The integrals above for n^* , K_0 and ξ can all be done analytically, and although simple asymptotic expansions can be made in various limits, we have found, unfortunately, that the regime relevant to current experiments requires the use of the full functional form. To simplify the notation somewhat, we introduce the auxiliary functions $C_0(z)$ and $D_0(z)$ where for $E_1(x) = \int_x^\infty t^{-1}e^{-t}dt$, we have

$$\begin{aligned} C_0(r_s, z) &= -1 + \frac{4E_1(z)}{(2 + \pi r_s)^2} + \frac{2e^{-z}r_s}{1 + 2r_s} \\ &\quad + (1 + 2zr_s)e^{2zr_s}(E_1[2zr_s] - E_1[z(1 + 2r_s)]), \quad (12.26) \\ D_0(r_s, z) &= 1 - \frac{8r_s z E_1[z]}{(2 + \pi r_s)^2} + \frac{8e^{-z}r_s}{(2 + \pi r_s)^2} - \frac{2e^{-z}r_s}{1 + 2r_s} \\ &\quad - 2zr_s e^{2zr_s}(E_1[2zr_s] - E_1[z(1 + 2r_s)]). \end{aligned}$$

Using these definitions, one finds [31]

$$\left. \begin{aligned} n^* &= 2 n_{\text{imp}} r_s^2 C_0, \\ K_0 &= \frac{1}{4r_s^2} \left(\frac{D_0}{C_0} \right)^2, \\ \xi &= \frac{1}{\sqrt{n_{\text{imp}}}} \frac{D_0}{4\pi r_s^2} (C_0)^{-3/2}, \end{aligned} \right\} \text{RPA} \quad (12.27)$$

where $z = 4d\sqrt{\pi n^*}$. Notice that given the concentration of charged impurities n_{imp} , the dielectric constant of the substrate (which sets r_s) and the distance d of the impurities from the graphene sheet, one can calculate the strength of the screened disorder potential, the size of the electron and hole puddles as well as the number of electrons within each puddle. In particular, we note that to leading order, the overall scale-factor of the puddle size is set by the average distance between the impurities $n_{\text{imp}}^{-1/2}$, and is proportional to r_s^{-2} . This allows one to make crude estimates, predicting, for example, that the size of the puddles in suspended graphene are roughly the same as those on a SiO_2 substrate. This is because although suspended graphene has more than an order of magnitude fewer impurities, one only gains as $n_{\text{imp}}^{-1/2}$, while suspending graphene more than doubles r_s , which decreases the puddle size as r_s^{-2} .

Notice that for the Complete Screening (CS) limit discussed earlier, the auxiliary functions have very simple asymptotes: $C_0(z \gg 1) \rightarrow (2r_s z)^{-2}$ and $D_0(z \gg 1) \rightarrow (2r_s z)^{-1}$. In this limit (which is valid only for very dirty samples when $d\sqrt{\pi n^*} \gg 1$), we find

$$\left. \begin{aligned} n^* &= \frac{1}{d} \sqrt{\frac{n_{\text{imp}}}{32\pi}}, \\ \xi &= d \sqrt{\frac{8}{\pi}}, \\ K_0 &= d \sqrt{8\pi n_{\text{imp}}}. \end{aligned} \right\} \begin{array}{l} \text{Complete} \\ \text{Screening} \end{array} \quad (12.28)$$

In Fig. 12.3 we show the function $C_0(z)$ for the RPA, Thomas-Fermi (TF) and Complete Screening (CS) approximations. For $z \gg 1$ the RPA and TF results approach the CS results, while in the opposite limit of $z \ll 1$, we have

$$C_0(r_s, z \rightarrow 0) = \frac{-1}{2r_s + 1} - \ln \left[\frac{2r_s}{2r_s + 1} \right] - \frac{4 \ln(\tilde{\gamma}z)}{(2 + \pi r_s)^2}, \quad (12.29)$$

where $\tilde{\gamma} \approx 1.781$ is Euler's constant. While using this asymptotic expression might be useful for qualitative estimates, we emphasize that in order to make any quantitative predictions, one is forced to use the full expression in Eq. 12.26.

Results

Having developed the self-consistent formalism above, we are now ready to reap some concrete results. Figure 12.4 captures the central results of the self-consistent approximation. The top panel shows the ensemble averaged two-point correlation function $\langle V(r)V(0) \rangle$. This quantity can be measured experimentally by measuring the density fluctuations at the Dirac point, although at present all the published experimental data lack sufficient resolution to make a detailed comparison. Nevertheless, they are at least consistent [34–37, 59] with the theoretical predictions. However, we can compare our results to those obtained using other theoretical approaches. The solid (blue) lines are the evaluation of Eq. 12.21 for two values of n_{imp} . The red diamonds are the results of the density function theory (DFT) taken from Ref. [32] using the same parameters. One notices that the self-consistent approximation (SCA) agrees quantitatively with the DFT results. The green line shows the Gaussian mapping which works remarkably well for the cleaner data. The full width at half maximum of $\langle V(r)V(0) \rangle$ (which is related to ξ through the Gaussian mapping) is a measure of the correlation length that sets the size of the puddles.

One of the main goals of developing the SCA was to calculate n_{rms} as a function of disorder parameters. This is shown in the right panel of Fig. 12.4 and Fig. 12.5, and these results also agree well with the DFT results [32]. Finally, in Fig. 12.6 we show the potential strength K_0 and puddle correlation length ξ (related to the puddle size) as a function of n_{imp} obtained by mapping the microscopic Coulomb disorder onto the Gaussian potential.

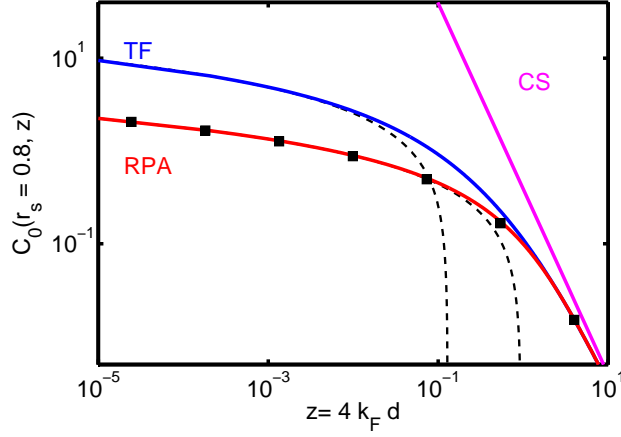


Fig. 12.3. Comparison of the dimensionless voltage fluctuation function $C_0(r_s, z)$ (see Eq. 12.26) using different screening approximations. The Random-Phase-Approximation (RPA) shown in blue is the main approximation used in the present work. The Thomas-Fermi (TF) and Complete Screening (CS) approximations give different results except when $r_s z \gg 1$. Dashed lines are small density analytic asymptotes for the Thomas-Fermi and RPA (see Eq. 12.29) and the squares show the numerical evaluation of Eq. 12.22 using the Coulomb potential (Eq. 12.11) with the exact dielectric function Eq. 12.9.

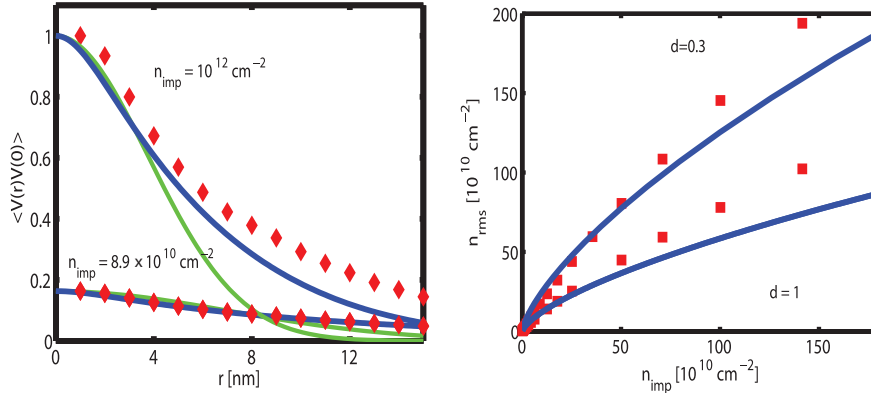


Fig. 12.4. Results of the self-consistent approximation (SCA). Left panel: Two-point correlation function of the screened Coulomb disorder potential. Blue line is the SCA result (Eq. 12.20), while green line is the Gaussian approximation (Eq. 12.23). The red data points taken from Ref. [32] show the same quantity computed from a density functional approach (see also discussion in Ref. [18]). Right panel: The root-mean-square carrier density at the Dirac point computed using the same approximations – blue line is the SCA (Eq. 12.24) and red squares are the DFT results (Ref. [32]).

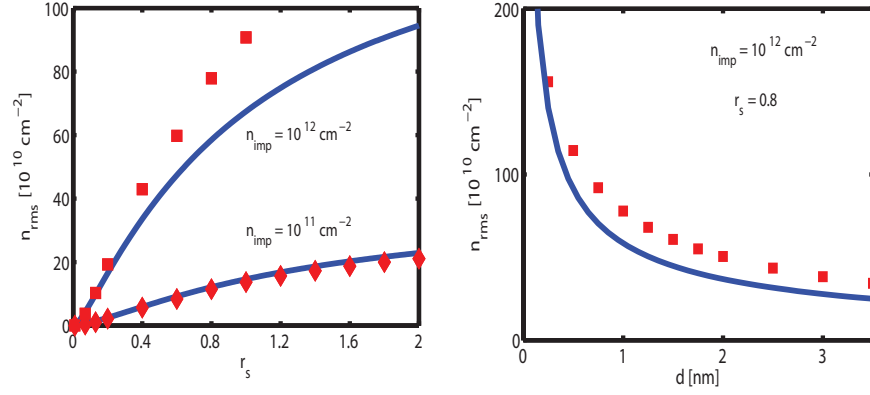


Fig. 12.5. Dependence of the carrier density fluctuations on effective fine structure constant r_s (left panel) and distance of the Coulomb impurities from the graphene sheet d (right panel). Solid lines are the self-consistent result (Eq. 12.20) and data points were computed in Ref. [32] using a density functional approach.

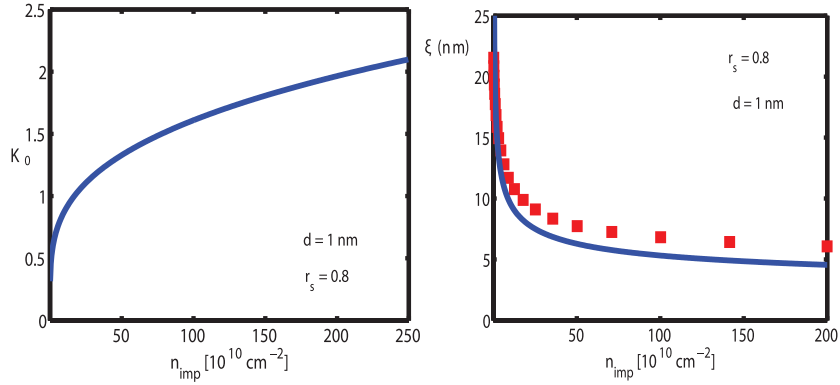


Fig. 12.6. Results for the Gaussian mapping of the Coulomb potential (see Eq. 12.23). Left panel shows the dimensionless disorder strength K_0 as a function of charged impurity density. Right panel shows the Gaussian correlation length ξ which is related to the average puddle size. Also shown as red squares is the density functional result of Ref. [32], where we note that for a Gaussian distribution function, a factor of $2\sqrt{2 \ln 2}$ needs to be multiplied by the correlation length ξ to obtain the full width at half maximum (FWHM) that is more commonly used to characterize the graphene puddles (see Ref. [18]).

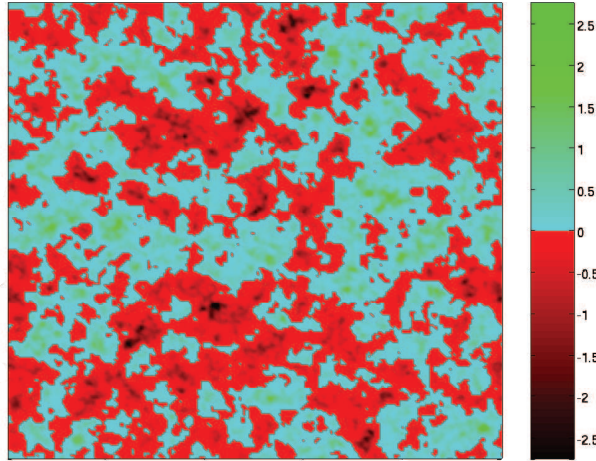


Fig. 12.7. At the Dirac point, disorder breaks the system into puddles of electrons and holes. The figure, taken from Ref. [63] is a simulation of a 250 nm by 250 nm square of graphene with typical density of charged impurities. The color scale reflects the local density in units of 10^{12} cm^{-2} . The goal of this section is to calculate the conductivity of this highly inhomogeneous material.

12.3.2 Effective medium theory

In the previous section we demonstrated that the self-consistent approximation can be used to quantify all the statistical properties of the Dirac point in the presence of disorder. For these dirty samples, the question now arises: given that we can characterize the Dirac point, what is the conductivity through this highly inhomogeneous medium? (See Fig. 12.7). Or in other words, now that we know the size of the puddles and how many carriers are inside the puddles, can we calculate the graphene minimum conductivity? The earliest (and crudest) estimate was simply to say that

$$\sigma \approx \begin{cases} \sigma_B(n^*) & \text{for } n \leq n^*, \\ \sigma_B(n) & \text{for } n > n^*, \end{cases} \quad (12.30)$$

where $\sigma_B(x) = 20(e^2/h)(x/n_{\text{imp}})$ [14]. We shall see in this section that this rather fortuitously turns out to be an excellent approximation.

The implication of Eq. 12.30 is the following: The disorder potential causes some residual carrier density n^* , which then gives rise to the minimum conductivity. As discussed in Sec. 12.3.1 above, n^* is determined by balancing the role of impurities doping graphene and the enhanced screening of doped graphene – but at a very basic level, it should be obvious that increasing the number of impurities increases n^* (see Fig. 12.4); which in turn should *increase* the conductivity. However, increasing n_{imp} also means more scattering which should *decrease* the conductivity. Therefore, the minimum conductiv-

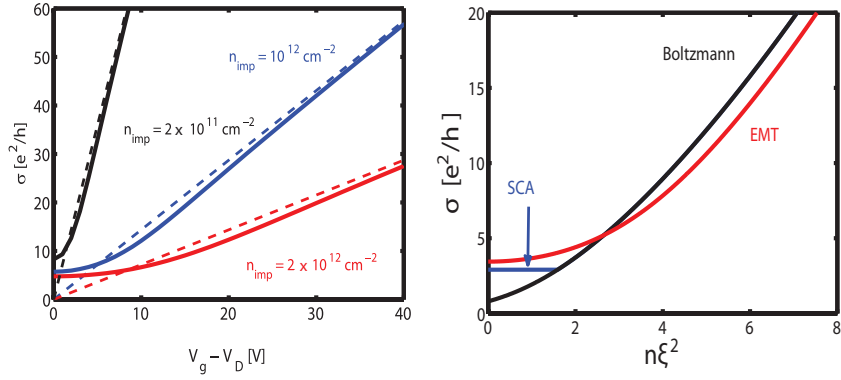


Fig. 12.8. Graphene conductivity as a function of carrier density for charged impurities (left panel) and Gaussian correlated impurities (right panel). Dashed lines in left panel are the high-density Boltzmann transport result. For Coulomb impurities (solid lines in left panel) the effective medium theory (EMT) results agree with the earlier estimate (Eq. 12.30) to within 1 %. For Gaussian impurities (right panel) the EMT gives slightly larger values for the minimum conductivity than Eq. 12.30. Also shown (in black) is the high-density Boltzmann result. The EMT result approaches the Boltzmann result for $n\xi^2 \gg 1$.

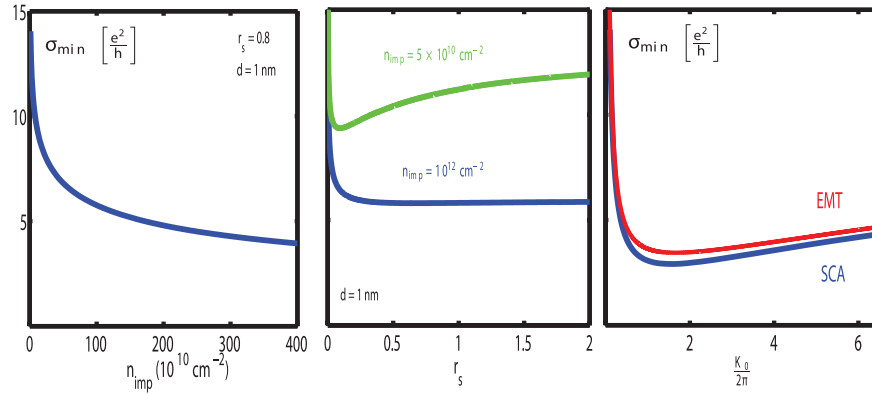


Fig. 12.9. Dependence of graphene minimum conductivity on disorder parameters. All panels have the same scale for σ_{min} on the y-axis. Left panel: For charged impurities, σ_{min} decreases monotonically as a function of impurity density. Center panel: Samples with large Coulomb disorder (blue curve) show almost no dependence of σ_{min} on the effective fine structure constant r_s ; cleaner samples (green curve) show the minimum conductivity increasing weakly with r_s . Right panel: For the Gaussian correlated impurity model, the effective medium theory result (Eq. 12.32) is slightly larger (red curve) than the analytic result $\sigma_{\text{min}}[x = K_0/2] = 2e^x/xI_1(x)$ shown in blue and derived from Eq. 12.30.

ity emerges as a delicate balance between the dual property of the disorder potential to both induce carriers and scatter carriers.

For the disorder concentrations present in the first experimental samples, these two effects roughly cancel resulting in a minimum conductivity that depends only weakly on disorder – and hence the early belief that the value was universal. For cleaner samples, the Coulomb impurity scattering term wins out, implying that cleaner samples should show stronger variation with disorder and have a larger value for σ_{\min} . (See Sec. 12.4 for further discussion of experiments).

Before we turn to the full treatment that validates the use of Eq. 12.30, let us look at what is obviously left out in this simple estimate. Since σ_B is the semi-classical Boltzmann conductivity, all quantum interference corrections are neglected. Sec. 12.3.4 below addresses quantum effects and studies the full crossover from quantum transport to diffusive transport. The approximation also assumes that the total conductivity is given by the conductivity within the puddles and not between puddles. As discussed earlier, this is justified because of the Klein tunneling across the p-n junctions. We refer the reader to Ref. [15] for more on the role of the boundary between the electron and hole puddles.

There are two further assumptions in Eq. 12.30. While one might buy that $\sigma_{\min} = \sigma_B(n^*)$, and $\sigma(n \gg n_{\text{imp}}) = \sigma_B(n)$, the hard “plateau” with a singularity at $n = n^*$ is highly artificial. Second, even the assumption that $\sigma_{\min} = \sigma_B(n^*)$ ignores the possibility that the minimum conductivity could depend on higher moments of the carrier density – for example, we could have proposed $\sigma_{\min} = \sigma_B(n_{\text{rms}})$ instead. Answering these two questions led to the development of an effective medium theory for graphene transport [38].

The starting point is to assume that locally $\sigma(r) = \sigma_B[n(r)]$. Then, taking the continuum approximation and using well-known effective medium theory (EMT) results [64] one finds [38]

$$\int dn P[n] \frac{\sigma(n) - \sigma_{\text{EMT}}}{\sigma(n) + \sigma_{\text{EMT}}} = 0, \quad (12.31)$$

where $P[n]$ is the carrier density probability distribution function. This integral equation for the conductivity of the inhomogeneous medium is valid so long as there are more than a few electrons inside each puddle. For current experiments on graphene, this is always the case. Theoretical calculations [32,38] showed that disordered graphene had two kinds of puddles – macroscopically large puddles with low carrier density that contained ≈ 500 electrons, and very small puddles with a large carrier density that contained ≈ 5 electrons. The statistics of these two regions were such that averaging over the entire sample gave results for the puddle correlation length ξ and n_{rms} that agreed with the self-consistent approximation discussed in the previous section. Making the further assumption that $P[n]$ is a Gaussian distribution with width n_{rms} and mean $n_g = \alpha V_g$, one finds [40]

$$\int_0^\infty \exp\left[\frac{-n^2}{2n_{\text{rms}}^2}\right] \cosh\left[\frac{n_g n}{n_{\text{rms}}^2}\right] \frac{\sigma(n) - \sigma_{\text{EMT}}}{\sigma(n) + \sigma_{\text{EMT}}} = 0. \quad (12.32)$$

To find the conductivity at the Dirac point, one sets the density induced by the back-gate voltage $n_g = 0$ giving for charged impurities

$$2ze^{-z^2} (\pi \text{Erfi}[z] - \text{Ei}[z^2]) = \sqrt{\pi}, \quad (12.33)$$

where Erfi is the imaginary error function, Ei is the exponential integral function and $z = \sigma_{\text{EMT}}/(\sqrt{2}\sigma_B[n_{\text{rms}}]) \approx 0.405$. This gives $\sigma_{\text{EMT}} \approx 0.9925 \sigma_B(n^*)$, implying that the early estimates for the minimum conductivity due to Coulomb scatterers (Eq. 12.30) were accurate to within 1 % of the effective medium theory result. However, with Eq. 12.32 one can now solve the full crossover of graphene conductivity as a function of carrier density from the Dirac point where the conductivity minimum is dominated by the contribution from the fluctuations in carrier density inside the electron and hole puddles to the high-density regime where the carrier density is uniform and the conductivity is given by the semiclassical Boltzmann results of Sec. 12.2.

Figure 12.8 shows the effective medium theory results $\sigma_{\text{EMT}}(n)$ for both Coulomb scatterers and Gaussian correlated impurities, where $n_{\text{rms}} = \sqrt{3}n^*$ was obtained from the self-consistent approximation. Fig. 12.9 shows the minimum conductivity σ_{min} for both Coulomb scatterers and for the Gaussian correlated impurity model. In Sec. 12.4 below we will compare the Coulomb impurity results (left panel of Fig. 12.9) to several experiments in the literature. Moreover, there has been some recent evidence that the predictions of the Gaussian impurity model (right panel of Fig. 12.9) are relevant for experiments doping graphene with atomic hydrogen [53], although there has been no microscopic theory explaining why hydrogen impurities should have such correlations.

12.3.3 Magneto-transport and temperature dependence of the minimum conductivity

One remarkable feature of this RPA-Boltzmann approach to solving the minimum conductivity problem is that the theory can then be generalized (without any further fitting parameters) to other experimental situations. The model makes definitive predictions for a variety of situations that have as yet not been explored theoretically using this technique (for example, the Nernst signal, the thermopower and weak-localization close to the Dirac point all in some way depend on the self-consistent carrier density n^* , which once determined through the dc transport, would then determine these additional properties). While we do not explore all these different experiments in this book chapter, it is relatively straightforward to generalize the formalism presented here to other situations. As an illustration of how such a generalization would work, we consider two cases here.

The first is the semi-classical magnetoresistance in a weak magnetic field, and the second is the temperature dependence of the minimum conductivity.⁹ The magneto-transport of graphene at sufficiently large temperatures that the phase-coherent transport is negligible and sufficiently small magnetic fields B such that Landau levels have not developed is given by the semi-classical Drude model. In graphene, the current density in the \hat{x} and \hat{y} directions is [43]

$$J_x = [\sigma_{xx}^{(e)} + \sigma_{xx}^{(h)}]E_x + [\sigma_{xy}^{(e)} + \sigma_{xy}^{(h)}]E_y; \quad J_y = [\sigma_{yx}^{(e)} + \sigma_{yx}^{(h)}]E_x + [\sigma_{yy}^{(e)} + \sigma_{yy}^{(h)}]E_y.$$

The superscript $c = (e, h)$ denotes electron and hole carriers. The longitudinal and Hall conductivities are given by

$$\sigma_{xx}^{(c)} = \sigma_{yy}^{(c)} = \frac{\sigma_0^{(c)}}{1 + \left(\sigma_0^{(c)} R_H^{(c)} B\right)^2}; \quad \sigma_{xy}^{(c)} = -\sigma_{yx}^{(c)} = \frac{\left[-\sigma_0^{(c)}\right]^2 R_H^{(c)} B}{1 + \left(\sigma_0^{(c)} R_H^{(c)} B\right)^2}, \quad (12.34)$$

where $R_H^{(c)} = 1/n_{(c)}e^{(c)}$ and the zero-field electrical conductivity for each carrier is $\sigma_0^{(c)}$. So far, this is general for any two carrier model.¹⁰ Applying the self-consistent theory simply gives $\sigma_0^{(e)} + \sigma_0^{(h)} = \sigma_{\text{EMT}}$, where σ_{EMT} is obtained from Eq. 12.32. This is an illustration of how the self-consistent theory can easily be generalized to other situations.

The second example we discuss here is the temperature dependence of the minimum conductivity. For simplicity, we assume the presence of only Coulomb scatterers and that the thermal smearing of the Fermi surface is the only source of temperature dependence. In this case, the local conductivity can be written as $\sigma(n, T) = n(T = 0)e\mu_c \frac{n_e + n_h}{n_e - n_h}$, where $n_e(T) =$

⁹ Here we assume that the temperature dependence arises only from thermal smearing of the Fermi distribution function. While this assumption that the temperature dependence occurs only from this activation-like behavior is an excellent approximation for bilayer graphene (see Ref. [40]), for monolayer graphene, additional physics such as the degradation of the conductivity due to phonons in dirty samples, and the crossover to the ballistic regime for suspended samples restrict the temperature range for which this thermal broadening picture dominates the conductivity.

¹⁰ As an aside, we should mention that the two carrier model above (and assuming Coulomb impurities, Eq. 12.12) relates field-effect mobility to the carrier mobility as

$$\mu_H \equiv \frac{\rho_{xy}}{\rho_{xx}B} = \frac{\sigma_{xy}}{\sigma_{xx}B} \approx \frac{A[r_s]}{n_{\text{imp}}} \left(\frac{n_e - n_h}{n_e + n_h} \right), \quad (12.35)$$

where only in the very limited carrier density range $n^* \sim n_{\text{imp}} \ll n \ll B[r_s]\sigma_0/n$ is the Hall mobility the same as the field-effect mobility $\mu_c = \sigma/ne$ (where the specific boundaries of this window depend on the number of short-range and long-range impurities and the dielectric environment).

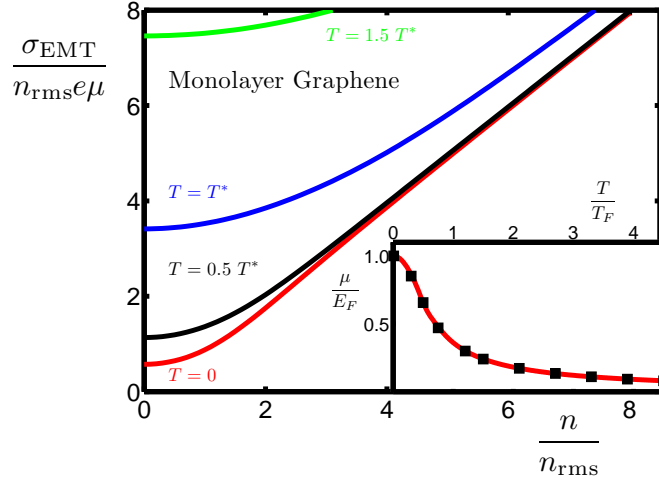


Fig. 12.10. Temperature dependence of graphene conductivity. Left panel shows effective medium theory conductivity for different values of $k_B T^* = \hbar v_F \sqrt{\pi n_{\text{rms}}}$, where n_{rms} is obtained from the self-consistent theory. Inset shows the chemical potential calculated numerically (squares) and the extrapolation function (Eq. 12.36) used to evaluate the conductivity. Perturbation theory for $t = T/T^* \ll 1$ gives $\sigma(t)/\sigma(0) = 1 + 4\pi^2 t^4 \ln t / (9|\pi - 2|)$.

$\int_0^\infty dE \nu(E) f(E, \mu, k_B T)$ and $n_h(T) = \int_{-\infty}^0 dE \nu(E) [1 - f(E, \mu, k_B T)]$ where $f(E, \mu, k_B T)$ is the Fermi-Dirac function with k_B the Boltzmann constant. The only subtle point is determining the chemical potential μ obtained by solving for $n_g = n_e - n_h$, where n_g is proportional to the applied gate voltage (and determined by the capacitive coupling of graphene to the gate). Data points in the inset of Fig. 12.10 show chemical potential $\mu(T)$ obtained by the numerical solution of the implicit equation, $1 = 2(T/T_F)^2 \{ \text{Li}_2[-\exp(\mu/k_B T)] - \text{Li}_2[-\exp(-\mu/k_B T)] \}$, as well as the interpolation function

$$F_\mu(x) = \mu(T/T_F)/E_F = g(x)(1 - \pi^2 x^2/6) + \bar{g}(x)/(4 \ln 2x), \quad (12.36)$$

where E_F is the Fermi energy, and $g(x) + \bar{g}(x) = 1$ are a choice of complementary functions, e.g. we use $g(x) = (1 + \text{Erf}[10(x - 1/2)])/2$ and $\bar{g}(x) = \text{Erfc}[10(x - 1/2)]/2$ [65]. From the inset, one finds that the interpolation function adequately describes the evolution of the chemical potential with temperature (see Ref. [40] for more details).

Applying the EMT formalism then gives the results shown in the left panel of Fig. 12.10. Since n_{rms} is obtained from the self-consistent approximation, this result gives a parameter free prediction for the effects of thermal broadening on the minimum conductivity.

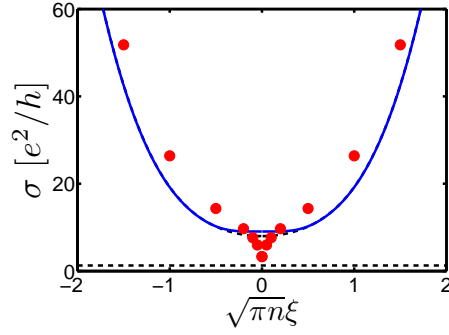


Fig. 12.11. Contrasting the quantum and semiclassical predictions for graphene Dirac point conductivity. Solid blue line is the semiclassical effective medium theory result which shows a smooth plateau close to the Dirac point. The dashed black curve is the Boltzmann result. The red data points represent the fully quantum transport result which shows a sharp dip at the Dirac point approaching the universal minimum value of $4e^2/\pi h$.

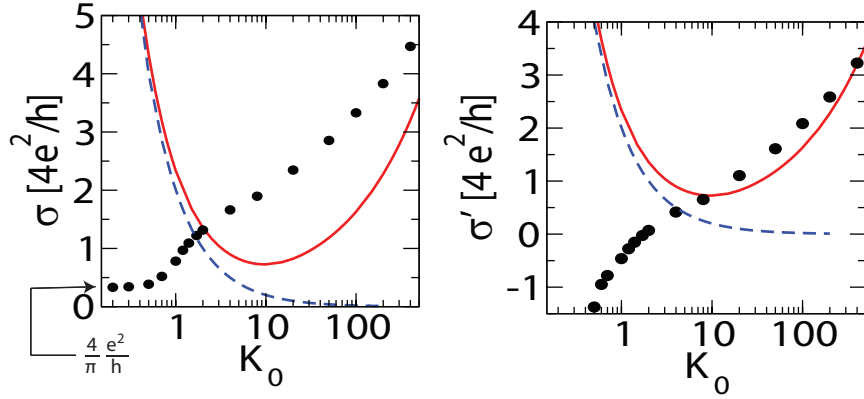


Fig. 12.12. Comparison of graphene conductivity calculated using the fully quantum theory and the semiclassical self-consistent approximation. The data points are the Landauer result (see Ref. [41]) while the solid red line is the SCA result (Eq. 12.30). The dashed blue line is the Boltzmann result which for this model has a minimum conductivity that scales as K_0^{-1} (see Eq. 12.18). For vanishing disorder, the quantum results give the universal value $\sigma_{\min} = 4e^2/\pi h$. With increasing disorder, the quantum results first increase sharply at $K_0 \approx 1$ followed by a more gradual increase for $K_0 \gtrsim 10$ (left panel). To test if this gradual increase is compatible with the self-consistent approximation, in the right panel we plot the classical component of the Landauer conductivity $\sigma' = \lim_{L \rightarrow \infty} [\sigma(L) - \pi^{-1} \ln(L/\xi)]$, where we have verified that for $\sigma \gtrsim 4e^2/h$ the L dependence is consistent with weak antilocalization. The fully quantum result agrees with the self-consistent approach when the number of electrons per puddle $N_e \approx \pi n^* \xi^2 = K_0/2\pi \gtrsim 1.6$.

12.3.4 Quantum to classical crossover

After the discovery of graphene, two parallel approaches developed to understand the conductivity of graphene. The first was the fully quantum-mechanical approach based on the Landauer formalism [66,67] where graphene was found to have a universal quantum-limited conductivity of $\sigma_{\min} = 4e^2/(\pi h)$, a value that was considerably lower than what was observed experimentally¹¹. While this formalism fully captures the quantum mechanics of graphene electrons, it ignores electron-interaction effects such as screening (discussed in Sec. 12.2.1 above). The natural question arises: can the discrepancy between the universal quantum-limited value and the value observed in experiments be caused by disorder? Early numerical work [25] suggested that this might be the case. At the time of writing this chapter, there has not been any convincing (or generally accepted) analytical model that addresses the role of disorder on the quantum-limited graphene conductivity at the charge neutrality point (see Ref. [15] for details). However, there have been (at least) five numerical studies [7, 16, 41, 68, 69] that have established that so long as the disorder is smooth on the scale of the lattice spacing, quantum interference effects *increase* the conductivity through weak anti-localization. We note that the presence of only smooth disorder (an assumption corroborated by graphene experimental STM studies [9, 37, 59, 60, 70] and TEM studies [71]) is necessary to ensure that the two graphene valleys are decoupled. Intervalley transitions break the pseudospin conservation resulting in the usual case of weak localization that decreases the conductivity signaling the transition to an insulating state [72].

The second approach was the semi-classical Boltzmann one described here. As discussed above the minimum conductivity depends on the delicate balance between the carrier density induced by the screened disorder potential and the carriers scattering off the same screened impurities. For Coulomb impurities, the scattering term always wins out, albeit only weakly at large disorder. As a result, for increased disorder, the minimum conductivity always *decreases*. This is in stark contrast to the predictions of the fully quantum approach.

Reference [41] attempted to reconcile these two approaches. The first step was to ensure that one was making a fair comparison. Since most of the quantum transport work in the literature was done with the Gaussian correlated impurity potential, the self-consistent approach first had to be generalized to this potential. In this chapter, the results for the Gaussian impurity model were already discussed alongside the Coulomb results in the preceding sections.

¹¹ The Landauer approach gives the universal value only for $W \gg L$, where the transport is primarily through evanescent modes. In the opposite limit, the conductivity depends strongly on the boundary conditions and is not universal. When comparing the quantum and semiclassical models, we will assume that $W \gg L$. For further discussion, see Ref. [15].

As can be observed in Fig. 12.9, the minimum conductivity for the Gaussian correlated potential makes a “U”-shape with a minimum at around $K_0 \approx 10$. The main findings of Ref. [41] were the following: (i) The numerical quantum results are consistent with weak-antilocalization theory (i.e. $d\sigma/d\ln L = 4e^2/\pi h$) at all carrier densities for $\sigma \geq 4e^2/h$. (ii) Away from the Dirac point, the full quantum solution and the semi-classical Boltzmann theory agree to leading order $\sigma \sim n^{3/2}$. Taken together with (i), this implies that outside the puddle regime, as one might expect, the graphene conductivity is determined by the semi-classical transport theory with small antilocalization corrections. (iii) At the Dirac point, the theories are incompatible at weak disorder ($K_0 \lesssim 10$) when quantum fluctuations spread the carriers over many puddles and the concept of a local carrier density becomes problematic. This is consistent with the discussion in Sec. 12.3.2 above, where we argued that the local density approach obviously fails when there are fewer than a couple of electrons per puddle. The number of electrons per puddle corresponds roughly to $\pi n^* \xi^2 = K_0/2\pi$, so this transition to the quantum regime occurs when there are fewer than 2 electrons per puddle. The experimental signature of the quantum regime is a sharp cusp-like dip at the Dirac point as opposed to the smooth plateau of the effective medium semiclassical theory (see Fig. 12.11). (iv) Most important, for the conductivity at the Dirac point, for $K_0 \gtrsim 10$ the quantum and the self-consistent theory agree (see Fig. 12.12, where in the right panel we subtract the antilocalization correction).

In the context of the results presented in this chapter, the consequence of Ref. [41] is that so long as the disorder is sufficiently large so that it induces more than a couple of electrons per puddle, the semi-classical transport theory effectively captures the transport properties of graphene and that additional physics that we have not considered such as the role of p-n junctions, are small corrections to our mean-field results.

12.3.5 Summary of theoretical predictions for Coulomb impurities

The material in this chapter has covered several different transport regimes including the full crossover from quantum transport to semi-classical transport, and several different impurity models from Coulomb scatterers to Gaussian correlated impurities. In this last section, we narrow our focus to consider the framework necessary to understand the initial graphene transport experiments. To this end, we specialize to the case of semi-classical transport in graphene with long-range Coulomb impurities. The impurity potential is fully specified by two parameters: The impurity concentration n_{imp} and the typical distance d between the impurities and the 2D graphene sheet. We use n_{imp} as the single parameter to distinguish various graphene experiments by fixing $d = 1$ nm, which is the correct order-of-magnitude for impurities either in the interfacial layer of the substrate or on top of the graphene sheet, and also fixing $r_s = 0.8$ which corresponds to the most common case of graphene on top of a SiO₂ substrate. We use two additional results (that due to space con-

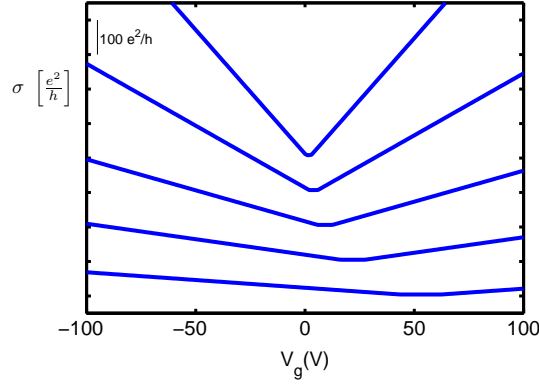


Fig. 12.13. Summary of theoretical predictions of the self-consistent approximation. Curves (from top to bottom) are for impurity density $n_{\text{imp}} = [20, 40, 80, 160, 320] \times 10^{10} \text{ cm}^{-2}$ and are offset by $100 e^2/h$ for clarity. The self-consistent theory [14] predicts that for charged impurity scattering, cleaner samples have (i) higher mobility, (ii) narrower minimum conductivity plateaus, (iii) smaller Dirac point offsets, and (iv) larger values for the minimum conductivity.

straints were not discussed elsewhere in this chapter): First, for $d \lesssim 1 \text{ nm}$, the high-density conductivity is only weakly dependent on d , and it is sufficient to use the analytic $d = 0$ result (Eq. 12.12). Second, as discussed in Sec. 12.3.1, once n^* is known, one can compute any moment of the disorder potential (see Eq. 12.22). In particular, the first moment $\langle V_D \rangle = n_{\text{imp}} \tilde{\phi}(q = 0)$ gives the shift of the Dirac point assuming that the disorder potential comprises only negatively charged impurities. Using the approximation of Eq. 12.30, we can summarize our results for graphene in a very compact analytical form [14]

$$\sigma(n - \bar{n}) = \begin{cases} \frac{20e^2}{h} \frac{n^*}{n_{\text{imp}}} & \text{if } n - \bar{n} < n^*, \\ \frac{20e^2}{h} \frac{n}{n_{\text{imp}}} & \text{if } n - \bar{n} > n^*, \end{cases} \quad (12.37)$$

$$\bar{n} = \frac{n_{\text{imp}}^2}{4n^*}, \quad \frac{n^*}{n_{\text{imp}}} = 2r_s^2 C_0 \left(r_s = 0.8, d = 1 \text{ nm}, a = 4d\sqrt{\pi n^*} \right) \quad (12.38)$$

$$C_0(r_s, a) = -1 + \frac{4E_1(a)}{(2 + \pi r_s)^2} + \frac{2e^{-a} r_s}{1 + 2r_s} + (1 + 2r_s a) e^{2r_s a} (E_1[2r_s a] - E_1[a(1 + 2r_s)]). \quad (12.39)$$

These theoretical predictions are shown in Fig. 12.13.

12.4 Comparison with experiments

In this brief section, we discuss only three experimental tests of the predictions made by the theory. In the literature, one can find several other examples

(some of which are discussed in the review article [15]). These three were picked as representative examples and are presented in chronological order. The important feature of all three experiments is that they span the full range of carrier density, thereby demonstrating that the physics at the Dirac plateau is governed by the same impurities that scatter carriers at high density where the semi-classical Boltzmann transport theory is expected to be a good approximation.

12.4.1 Magnetotransport: dependence of σ_{xx} and σ_{xy} on carrier density

The first test of the self-consistent theory was done in Ref. [43] by comparing with experimental data from the Manchester group [42]. The zero-magnetic-field experimental data was compared to the theory Eq. 12.37 and determined $n_{\text{imp}} \approx 1.75 \times 10^{12} \text{ cm}^{-2}$. This fit and the experimental data are shown in the inset of Fig. 12.15. The experimental data for the longitudinal resistivity ρ_{xx} and Hall resistivity ρ_{xy} at $B = 1 \text{ T}$ was compared to the theoretical predictions given by Eq. 12.34 without introducing any additional fitting parameters. Since the experimentalists subtracted the Dirac point offset when taking the measurements, we could not test the additional prediction in Eq. 12.37 for the impurity induced Dirac point shift. Nonetheless the agreement for the full magneto-transport data with a single fit parameter is quite remarkable.

12.4.2 Dependence of σ_{min} and mobility on impurity concentration

The theory presented here makes very specific predictions for the dependence of the minimum conductivity on impurity density. In the right panel of Fig. 12.15 we compare the theoretical results for $\sigma_{\text{min}}(n_{\text{imp}})$ with several different experimental data sets from various groups. We emphasize that there has been no arbitrary selection of data for this figure, it represents *all* the four-probe data sets for graphene on a SiO_2 substrate for which we have done a detailed comparison between theory and experiment.

The data from the Columbia group are the same samples that were analyzed in Ref. [13], where the values of n_{imp} were obtained from fitting the high-density data and the shift of the Dirac point. The upward triangles are data from the Manchester group [10, 42], diamonds from the Maryland group [73] and the downward triangle taken from Ref. [74]. In all these samples, the value of n_{imp} is determined by fitting the high-density transport data. The black circles show the potassium doping experiments of Ref. [44], where charged impurities were intentionally added to graphene. The data shown here are for the initial deposition of the charged impurities on graphene. After annealing the sample, the subsequent runs showed different behavior suggesting the correlation between the impurity atoms. Our treatment here has been for uncorrelated impurities (see Eq. 12.21), although it is worth mentioning that it is relatively straightforward to generalize our formalism to the case of correlated

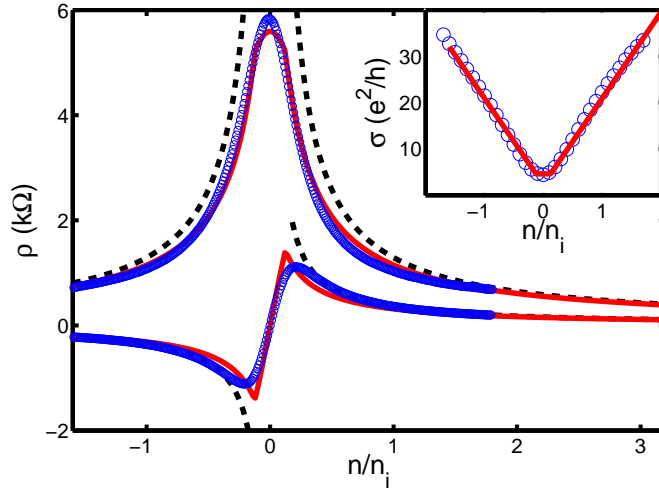


Fig. 12.14. Comparison of theoretical predictions for magneto-transport with experimental results. Red curves are Eq. 12.34 and Eq. 12.37 using the single fit parameter $n_{\text{imp}} \approx 1.75 \times 10^{12} \text{ cm}^{-2}$. Blue circles are experimental data at $B = 1T$. Dashed lines show the Boltzmann transport result without the self-consistent correction that diverges at low carrier density. Inset: Conductivity data for the same sample at $B = 0 \text{ T}$.

impurities if the distribution of the impurity positions is known. Subsequent experiments [75] using transition metal impurities instead of potassium also showed agreement with the theory before annealing, followed by an increase in conductivity after annealing, suggestive of impurity correlations. If the resultant potential fluctuations can be characterized by the Gaussian model (see Eq. 12.23), we speculate that the results shown in Fig. 12.9 should apply, and in particular, that the minimum conductivity would be a non-monotonic function of the impurity density. In any case, the agreement between theory and experiment shown in Fig. 12.15 is strong evidence both for the dominant role of Coulomb impurities and that the physics of the minimum conductivity is captured by the self-consistent approximation.

12.4.3 Dependence of σ_{min} and mobility on dielectric environment

Perhaps the most precise test of the theory presented here was done in Ref. [28]. In this experiment the graphene conductivity was first measured in ultra-high vacuum (UHV) and fit to the Boltzmann theory discussed here for short-range and Coulomb impurities. Unlike the experiments discussed in Sec. 12.2.6, this combination of weak impurities provides a better description than the strong impurity model.

Several monolayers of ice were then introduced to the sample until there were no further changes in the transport properties. Since the dielectric con-

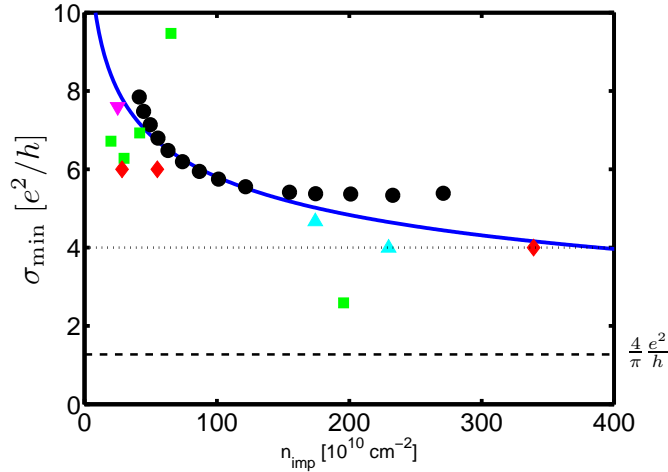


Fig. 12.15. Dependence of graphene minimum conductivity on charged impurity density. Experimental data is taken from Columbia (squares), Exeter (downward triangle), Manchester (upward triangles) and Maryland (diamonds and circles) (see text for details). The solid blue theoretical curve is the same as in the left panel of Fig. 12.9. The dashed horizontal line shows the universal quantum limited value of $\sigma_{\min} = (4/\pi)e^2/h$ and the dotted horizontal line shows $\sigma = 4e^2/h$ that was observed in the earlier experiments on dirtier samples.

stant for vacuum, SiO_2 and ice are all known, the theory makes predictions for the changes in conductivity with *no free parameters*. In particular, it predicts that the low density mobility should *increase* by 26 % (Fig. 12.2) and the high density conductivity should *decrease* by 38 % (Fig. 12.2) and that the minimum conductivity (Fig. 12.9) should *decrease* by 0.01 % (i.e. stay unchanged). The experiments found the mobility increased by (31 ± 1) %, the high density conductivity decreased by (38 ± 1) %, and the minimum changed by (0 ± 0.1) %, in excellent agreement with the theory. This experiment demonstrated that the theory presented in this chapter works to within a 5 % accuracy for large 4-probe samples in UHV. Reports using liquid dielectrics at room temperature and pressure are more ambiguous [76]. While these experiments qualitatively show the predicted trends for Coulomb and short-range impurities [77], quantitative comparisons are more difficult for several reasons. For example, one is often at high enough carrier densities that the opposing effects of long-range and short-range impurities result in only small changes to the conductivity. Also, the ions in solution could themselves act as additional charged impurities.

Focusing on the UHV results, in Fig. 12.16 we compare the theoretical predictions against the experimental data. Again, the theory has no fitting parameters, and captures not only the high and low density behavior (discussed above), but also the crossover from when Coulomb scatterers dominate

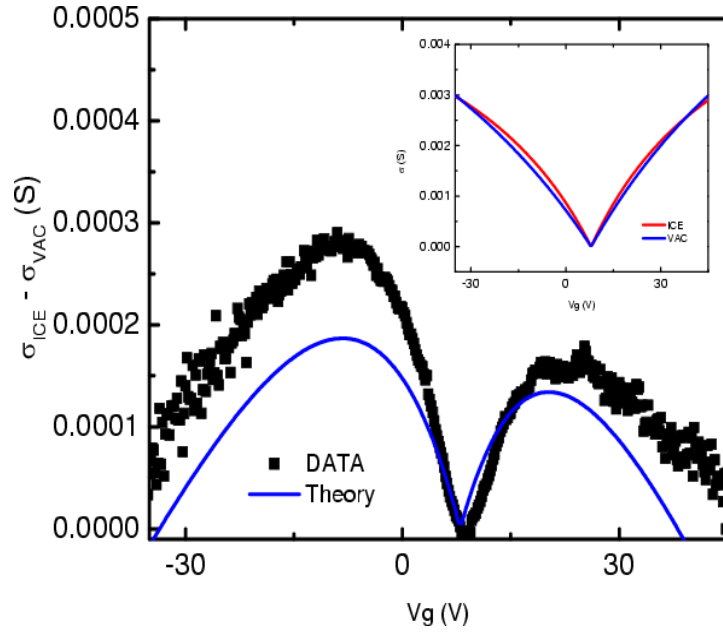


Fig. 12.16. Comparison of experimental data and theoretical predictions for $\sigma_{\text{ice}} - \sigma_{\text{vac}}$. Since the dielectric constants of vacuum, ice and SiO_2 are known, the theory has no adjustable parameters. Inset shows the experimental data. This figure was adapted from Ref. [28].

to when short-range scatterers dominate (as reflected in the non-monotonicity of the curve). We point out that both the theoretical and experimental curves cross the x-axis at particular carrier densities. If one were to perform the same experiment sitting close to that point, then theory predicts that one would observe no changes in the conductivity when changing the dielectric constant, as discussed above in the context of liquid dielectrics.

12.5 Conclusion

In this chapter we have tried to provide a concise description of the different physical mechanisms at play in a typical graphene transport experiment. On one hand, since the carrier transport involves quantum mechanical tunneling and scattering, many-body interaction effects, and strong disorder induced spatial inhomogeneities, as well as the absence of a natural perturbation parameter, the problem could have been completely intractable. However, it seems that for this first practical realization of Dirac fermions in a condensed matter system, nature was rather kind. Exfoliated graphene sits at a particular sweet-spot, where although each of the mechanisms are important, and none can be neglected, they are each very weak and can be treated to high

accuracy within their simplest models. What matters then is not exploring any one constituent part to higher accuracy, but rather to understand the interplay between these mechanisms and the various competitions that give rise to the unusual transport properties in graphene.

For example, we have seen that graphene's minimum conductivity is a balance between how many carriers are induced by the disorder and how the disorder then scatters these carriers. The number of carriers induced by the disorder is in turn a feedback loop where a strong disorder potential induces more carriers which makes graphene better able to screen external potentials thereby weakening the effective disorder potential. And it is the highly efficient quantum tunneling between the electron and hole puddles that allows one to ignore the quantum transport and use the semi-classical effective medium theory.

It is primarily because graphene is perched at the intersection of these different influences that the minimum conductivity seems so insensitive to perturbations. In Fig. 12.9 we show that changing the disorder concentration by more than two orders of magnitude changes the value of σ_{\min} by a factor of less than 3. In the same figure we see that for typical disorder concentrations, changing the dielectric constant from 1 (vacuum) to 8 hardly changes σ_{\min} . But the theory also contains the limits. When the disorder is reduced such that the mean-free-path becomes longer than the distance between the contacts, then the quantum-limited (and universal) minimum conductivity of $\sigma_{\min} = 4e^2/\pi h$ should emerge. Achieving this is simpler than one might imagine – rather than looking for cleaner samples, one just needs to make closer contacts. Similarly, for graphene, we have $r_s \leq 2$ so that interaction effects are weak. But strained graphene or graphene in a large magnetic field, or some of the new Dirac fermion systems found on the surface of topological insulators have stronger interactions. There will certainly continue to be exciting new directions and ever-more exotic mechanisms to be discovered in graphene transport experiments in the future; however, we remain convinced that these will be observed as strong deviations from the weak coupling theory presented here.

Acknowledgement. Most of the research leading up to the material covered in this chapter was done while I was a postdoctoral research associate with the Condensed Matter Theory Center at the University of Maryland under the mentorship of Sankar Das Sarma, where it was supported by U.S. ONR, and the NSF-NRI-SWAN. During this time I also benefited enormously from collaborations with Michael Fuhrer, Euyheon Hwang, Enrico Rossi, Victor Galitski and Ellen Williams. Some of the more recent work was done with Piet Brouwer, Mark Stiles and Parakh Jain. I am also grateful to Mark Stiles, Michael Fuhrer, Jabez McClelland, Joseph Stroschio, Hongki Min, Hassan Raza, and Nikolai Zhitenev for their valuable comments.

References

1. C. Lee, X. Wei, J.W. Kysar, J. Hone, *Science* **321**, 385 (2008)
2. Y.M. Lin, C. Dimitrakopoulos, K.A. Jenkins, D.B. Farmer, H.Y. Chiu, A. Grill, P. Avouris, *Science* **327**(5966), 662 (2010)
3. J.H. Chen, C. Jang, S. Xiao, M. Ishigami, M.S. Fuhrer, *Nature Nanotechnology* **3**, 206 (2008)
4. S. Bae, H. Kim, Y. Lee, X. Xu, J.S. Park, Y. Zheng, J. Balakrishnan, T. Lei, H.R. Kim, Y.I. Song, Y.J. Kim, K.S. Kim, B. Ozyilmaz, J.H. Ahn, B.H. Hong, S. Iijima, *Nature Nanotechnology* **5**(8), 574 (2010)
5. D.E. Sheehy, J. Schmalian, *Phys. Rev. Lett.* **99**(22), 226803 (2007)
6. M.S. Fuhrer, S. Adam, *Nature* **458**(7234), 38 (2009)
7. J.H. Bardarson, J. Tworzydło, P.W. Brouwer, C.W.J. Beenakker, *Phys. Rev. Lett.* **99**, 106801 (2007)
8. C.L. Kane, E.J. Mele, *Phys. Rev. Lett.* **95**(14), 146802 (2005)
9. Y.J. Song, A.F. Otte, Y. Kuk, Y. Hu, D.B. Torrance, P.N. First, W.A. de Heer, H. Min, S. Adam, M.D. Stiles, A.H. MacDonald, J.A. Stroscio, *Nature* **467**, 185 (2010)
10. K.S. Novoselov, A.K. Geim, S.V. Morozov, D. Jiang, Y. Zhang, S.V. Dubonos, I.V. Grigorieva, A.A. Firsov, *Science* **306**, 666 (2004)
11. K.S. Novoselov, A.K. Geim, S.V. Morozov, D. Jiang, Y. Zhang, M.I. Katsnelson, I.V. Grigorieva, S.V. Dubonos, A.A. Firsov, *Nature* **438**, 197 (2005)
12. Y. Zhang, Y.W. Tan, H.L. Stormer, P. Kim, *Nature* **438**, 201 (2005)
13. Y.W. Tan, Y. Zhang, K. Bolotin, Y. Zhao, S. Adam, E.H. Hwang, S. Das Sarma, H.L. Stormer, P. Kim, *Phys. Rev. Lett.* **99**(24), 246803 (2007)
14. S. Adam, E.H. Hwang, V.M. Galitski, S. Das Sarma, *Proc. Natl. Acad. Sci. USA* **104**, 18392 (2007)
15. S. Das Sarma, S. Adam, E.H. Hwang, E. Rossi, *Rev. Mod. Phys.* (in press); arXiv:1003.4731 (2011)
16. E.R. Mucciolo, C.H. Lewenkopf, *Journal of Physics: Condensed Matter* **22**(27), 273201 (2010)
17. N.M.R. Peres, *Rev. Mod. Phys.* **82**(3), 2673 (2010)
18. S. Adam, E.H. Hwang, E. Rossi, S. Das Sarma, *Solid State Commun.* **149**, 1072 (2009)
19. A.W.W. Ludwig, M.P.A. Fisher, R. Shankar, G. Grinstein, *Phys. Rev. B* **50**(11), 7526 (1994)
20. N. Shon, T. Ando, *J. Phys. Soc. Jpn.* **67**, 2421 (1998)
21. T. Ando, *J. Phys. Soc. Jpn.* **75**, 074716 (2006)
22. E.H. Hwang, S. Das Sarma, *Phys. Rev. B* **75**, 205418 (2007)
23. B. Wunsch, T. Stauber, F. Sols, F. Guinea, *New J. Phys.* **8**, 318 (2006)
24. M. Polini, R. Asgari, Y. Barlas, T. Pereg-Barnea, A. MacDonald, *Solid State Commun.* **143**, 58 (2007)
25. K. Nomura, A.H. MacDonald, *Phys. Rev. Lett.* **98**, 076602 (2007)
26. E.H. Hwang, S. Adam, S. Das Sarma, *Phys. Rev. Lett.* **98**, 186806 (2007)
27. M. Trushin, J. Schliemann, *Phys. Rev. Lett.* **99**, 216602 (2007)
28. C. Jang, S. Adam, J.H. Chen, E.D. Williams, S. Das Sarma, M.S. Fuhrer, *Phys. Rev. Lett.* **101**(14), 146805 (2008)
29. S. Adam, E. Hwang, S. Das Sarma, *Physica E* **40**, 1022 (2008)
30. T. Stauber, N.M.R. Peres, F. Guinea, *Phys. Rev. B* **76**(20), 205423 (2007)

31. S. Adam, S. Cho, M.S. Fuhrer, S. Das Sarma, Phys. Rev. Lett. **101**, 046404 (2008)
32. E. Rossi, S. Das Sarma, Phys. Rev. Lett. **101**(16), 166803 (2008)
33. M. Polini, A. Tomadin, R. Asgari, A.H. MacDonald, Phys. Rev. B **78**(11), 115426 (2008)
34. J. Martin, N. Akerman, G. Ulbricht, T. Lohmann, J.H. Smet, K. von Klitzing, A. Yacobi, Nature Physics **4**, 144 (2008)
35. A. Deshpande, W. Bao, F. Miao, C.N. Lau, B.J. LeRoy, Phys. Rev. B **79**(20), 205411 (2009)
36. Y. Zhang, V. Brar, C. Girit, A. Zettl, M. Crommie, Nature Physics **5**, 722 (2009)
37. D. Miller, K. Kubista, G. Rutter, M. Ruan, W. de Heer, P. First, J. Stroscio, Science **324**, 924 (2009)
38. E. Rossi, S. Adam, S. Das Sarma, Phys. Rev. B **79**(24), 245423 (2009)
39. M.M. Fogler, Phys. Rev. Lett. **103**, 236801 (2009)
40. S. Adam, M.D. Stiles, Phys. Rev. B **82**(7), 075423 (2010)
41. S. Adam, P.W. Brouwer, S. Das Sarma, Phys. Rev. B **79**(20), 201404 (2009)
42. F. Schedin, A.K. Geim, S.V. Morozov, D. Jiang, E.H. Hill, P. Blake, K.S. Novoselov, Nature Materials **6**, 652 (2007)
43. E.H. Hwang, S. Adam, S. Das Sarma, Phys. Rev. B **76**(19), 195421 (2007)
44. J.H. Chen, C. Jang, S. Adam, M.S. Fuhrer, E.D. Williams, M. Ishigami, Nature Physics **4**, 377 (2008)
45. N.W. Ashcroft, N.D. Mermin, *Solid State Physics* (Saunders, 1976)
46. H. Bruus, K. Flensberg, *Many-Body Quantum Theory in Condensed Matter Physics: An Introduction* (Oxford University Press, Oxford, 2004)
47. A. Ferreira, J.V. Gomes, J. Nilsson, E.R. Mucciolo, N.M.R. Peres, A.H. Castro Neto, arXiv:1010.4026v1 (2010)
48. J. Gonzalez, F. Guinea, V.A.M. Vozmediano, Nucl. Phys. B **424**, 595 (1994)
49. T. Ando, A.B. Fowler, F. Stern, Rev. Mod. Phys. **54**, 437 (1982)
50. K. Bolotin, K. Sikes, Z. Jiang, G. Fudenberg, J. Hone, P. Kim, H. Stormer, Solid State Commun. **146**, 351 (2008)
51. S. Adam, S. Das Sarma, Solid State Commun. **146**, 356 (2008)
52. C.H. Lewenkopf, E.R. Mucciolo, A.H. Castro Neto, Phys. Rev. B **77**, 081410 (2008)
53. J. Katoch, J. Chen, R. Tsuchikawa, C. Smith, E.R. Mucciolo, M. Ishigami, Phys. Rev. B **82**(8), 081417 (2010)
54. T.O. Wehling, S. Yuan, A.I. Lichtenstein, A.K. Geim, M.I. Katsnelson, Phys. Rev. Lett. **105**(5), 056802 (2010)
55. Z.H. Ni, L.A. Ponomarenko, R.R. Nair, R. Yang, S. Anissimova, I.V. Grigorieva, F. Schedin, P. Blake, Z.X. Shen, E.H. Hill, K.S. Novoselov, A.K. Geim, Nano Lett. **10**, 3868 (2010)
56. M. Hentschel, F. Guinea, Phys. Rev. B **76**, 115407 (2007)
57. J.H. Chen, W.G. Cullen, C. Jang, M.S. Fuhrer, E.D. Williams, Phys. Rev. Lett. **102**, 236805 (2009)
58. V. Ugarte, V. Aji, C.M. Varma, arXiv:1007.3533 (2010)
59. S. Jung, G.M. Rutter, N.N. Klimov, D.B. Newell, I. Calizo, A.R. Hight-Walker, N.B. Zhitenev, J.A. Stroscio, Nat. Phys. (in press); arXiv:1011.0888 (2011)
60. M. Ishigami, J.H. Chen, W.G. Cullen, M.S. Fuhrer, E.D. Williams, Nano Lett. **7**, 1643 (2007)
61. S. Das Sarma, M.P. Lilly, E.H. Hwang, L.N. Pfeiffer, K.W. West, J.L. Reno, Phys. Rev. Lett. **94**(13), 136401 (2005)

62. V. Galitski, S. Adam, S. Das Sarma, Phys. Rev. B **76**(24), 245405 (2007)
63. E. Rossi, private communication (2008)
64. R. Landauer, J. Appl. Phys. **23**, 779 (1952)
65. I.S. Gradshteyn, I.M. Ryzhik, *Table of integrals, series, and products*, 5th edn. (Academic Press, 1994)
66. M.I. Katsnelson, Eur. Phys. J. B **51**, 157 (2006)
67. J. Tworzydło, B. Trauzettel, M. Titov, A. Rycerz, C.W.J. Beenakker, Phys. Rev. Lett. **96**(24), 246802 (2006)
68. K. Nomura, M. Koshino, S. Ryu, Phys. Rev. Lett. **99**, 146806 (2007)
69. P. San-Jose, E. Prada, D.S. Golubev, Phys. Rev. B **76**, 195445 (2007)
70. A. Luican, G. Li, E.Y. Andrei, Solid State Commun. **149**, 1151 (2009)
71. J.C. Meyer, C. Kisielowski, R. Erni, M.D. Rossell, M.F. Crommie, A. Zettl, Nano Lett. **8**, 3582 (2008)
72. H. Suzuura, T. Ando, Phys. Rev. Lett. **89**(26), 266603 (2002)
73. J.H. Chen, C. Jang, M. Ishigami, S. Xiao, W. Cullen, E. Williams, M. Fuhrer, Solid State Commun. **149**(27-28), 1080 (2009)
74. F.V. Tikhonenko, A.A. Kozikov, A.K. Savchenko, R.V. Gorbachev, Phys. Rev. Lett. **103**, 226801 (2009)
75. K. Pi, K.M. McCreary, W. Bao, W. Han, Y.F. Chiang, Y. Li, S.W. Tsai, C.N. Lau, R.K. Kawakami, Phys. Rev. B **80**(7), 075406 (2009)
76. L.A. Ponomarenko, R. Yang, T.M. Mohiuddin, M.I. Katsnelson, K.S. Novoselov, S.V. Morozov, A.A. Zhukov, F. Schedin, E.W. Hill, A.K. Geim, Phys. Rev. Lett. **102**, 206603 (2009)
77. K. Novoselov, private communication (2009)